J. Fluid Mech. (2023), *vol*. 974, A47, doi:10.1017/jfm.2023.783

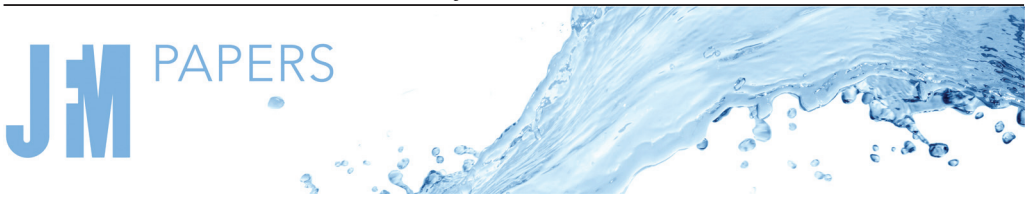

Large-scale streaks in a turbulent bluff body wake

Akhil Nekkanti[1],‡, **Sheel Nidhan**[1], **Oliver T. Schmidt**[1] **and Sutanu Sarkar**[1],†

[1]Department of Mechanical and Aerospace Engineering, University of California San Diego, CA 92093, USA

(Received 17 April 2023; revised 28 July 2023; accepted 9 September 2023)

A turbulent circular disk wake database (Chongsiripinyo & Sarkar, *J. Fluid Mech.*, vol. 885, 2020) at Reynolds number $Re = U_\infty D/\nu = 5 \times 10^4$ is interrogated to identify the presence of large-scale streaks – coherent elongated regions of streamwise velocity. The unprecedented streamwise length – until $x/D \approx 120$ – of the simulation enables investigation of the near and far wakes. The near wake is dominated by the vortex shedding (VS) mode residing at azimuthal wavenumber $m = 1$ and Strouhal number $St = 0.135$. After filtering out the VS structure, conclusive evidence of large-scale streaks with frequency $St \to 0$, equivalently streamwise wavenumber $k_x \to 0$ in the wake, becomes apparent in visualizations and spectra. These streaky structures are found throughout the simulation domain beyond $x/D \approx 10$. Conditionally averaged streamwise vorticity fields reveal that the lift-up mechanism is active in the near as well as the far wake, and that ejections contribute more than sweeps to events of intense $-u_x' u_r'$. Spectral proper orthogonal decomposition is employed to extract the energy and the spatiotemporal features of the large-scale streaks. The streak energy is concentrated in the $m = 2$ azimuthal mode over the entire domain. Finally, bispectral mode decomposition is conducted to reveal strong interaction between $m = 1$ and $St = \pm 0.135$ modes to give the $m = 2$, $St \to 0$ streak mode. Our results indicate that the self-interaction of the VS mode generates the $m = 2$, $St \to 0$ streamwise vortices, which leads to streak formation through the lift-up process. To the authors' knowledge, this is the first study that reports and characterizes large-scale low-frequency streaks and the associated lift-up mechanism in a turbulent wake.

Key words: wakes

1. Introduction

Coherent structures, which are organized patterns of motion in a seemingly random turbulent flow field, play an essential role in turbulent shear flows. Among these structures,

† Email address for correspondence: sarkar@ucsd.edu
‡ Present address: Division of Engineering and Applied Science, California Institute of Technology, Pasadena, CA 91125, USA.

streaks are among the most widely discussed, particularly in wall-bounded flows, where they were identified experimentally (Kline *et al.* 1967) as elongated regions of streamwise velocity in the near-wall region. As these streaks break up, they transfer energy from the inner to the outer layers, thereby maintaining turbulence in the outer layers of the boundary layer (Kim, Kline & Reynolds 1971). This process, also known as bursting, can account for up to 75 % of Reynolds stresses (Lu & Willmarth 1973), hence assisting in the production of turbulent kinetic energy (TKE). Smith & Metzler (1983) found that low-speed streaks are robust features of boundary layers, occurring across a wide range of Reynolds numbers ($740 < Re_\theta < 5830$). Their spanwise spacing of 100 wall units was found to be invariant with Re_θ. Hutchins & Marusic (2007) investigated the logarithmic region of the boundary layer, finding that the streaks in this region are distinct and much larger than the near-wall streaks, extending up to 20 times the boundary layer thickness. Building upon this work, Monty *et al.* (2007) reported the existence of streaks in the logarithmic region of turbulent pipe and channel flows as well. They also found that the width of these structures in channel and pipe flows is larger than that of the boundary layer.

The presence of a wall is not a prerequisite for the formation of streaks (Jiménez & Pinelli 1999; Mizuno & Jiménez 2013). A few studies in the past, such as Brown & Roshko (1974) (see figure 8*b*), Bernal & Roshko (1986) and Liepmann & Gharib (1992), have reported the presence of streak-like structures in the mixing layer, with the latter two showing increasing amplification of the streaks as the flow progresses downstream. Recently, more attention has been paid to the role of streaks in the mixing layer and especially the jet. Jiménez-González & Brancher (2017) performed transient growth analysis in round jets, finding that for optimal initial disturbances, the streamwise vortices evolve to produce streamwise streaks. Marant & Cossu (2018) also reported similar findings in a hyperbolic-tangent mixing layer. Nogueira *et al.* (2019) applied spectral proper orthogonal decomposition (SPOD) on a particle image velocimetry dataset of a circular turbulent jet at a high Reynolds number, and demonstrated the presence of large-scale streaky structures in the near field (until $x/D = 8$). They demonstrated further that these structures exhibit large time scales and are associated with a low frequency, $St \to 0$. The numerical counterpart of the previous study was performed by Pickering *et al.* (2020). They found that the streaky structures near the nozzle exit are dominated by higher azimuthal wavenumbers, and the dominance shifts to lower azimuthal wavenumbers downstream, with $m = 2$ dominating by $x/D = 30$. A similar conclusion about the dominance of $m = 2$ was reached by Samie *et al.* (2022) who utilized quadrant analysis on a low-Reynolds-number jet.

In wall-bounded flows, streaks are generated by the lift-up mechanism (Ellingsen & Palm 1975; Landahl 1975). Streamwise vortices induce wall-normal velocities, bringing fluid from high-speed to low-speed regions, and vice versa, to form streaks, hence the term 'lift-up'. The subsequent instability and breakdown of these streaks are important to the self-sustaining cycle of wall turbulence (Hamilton, Kim & Waleffe 1995; Waleffe 1997). Brandt (2014) presents a detailed review of the theory behind the lift-up mechanism and its role in transitional and turbulent flows. Although originally introduced as an instability mechanism that destabilizes a streamwise-independent base flow, the lift-up mechanism has been found to be dynamically crucial to fully turbulent wall-bounded flows as well (Farrell & Ioannou 2012; Jiménez 2018; Bae, Lozano-Duran & McKeon 2021).

The lift-up mechanism is active and plays a critical role in jets too. In their resolvent analysis of data from a turbulent jet experiment, Nogueira *et al.* (2019) found that the optimal forcing modes at $St \to 0$ take the form of streamwise vortices that eject high-speed fluid and sweep low-speed fluid, depending on the orientation of these vortices. Pickering

et al. (2020) analysed a turbulent jet large eddy simulations (LES) database, finding that the response modes of these lift-up-dominated optimal forcing modes indeed take the form of streamwise streaks. While these studies focused on circular jets, Lasagna, Buxton & Fiscaletti (2021) found that the lift-up mechanism is active in the near field of fractal jets as well.

As discussed above, there has been growing interest in the investigation of streaky structures and lift-up mechanisms in free shear flows, particularly in turbulent jets. These experimental and numerical studies have confirmed that the presence of a wall is not necessary for the formation of streaks, which has motivated us to explore another important class of free shear flows, i.e. turbulent wakes. Previous wake studies have focused primarily on the vortex shedding (VS) mechanism. Near the body and in the intermediate wake, the VS mode emerges as the most dominant coherent structure (Taneda 1978; Berger, Scholz & Schumm 1990; Cannon, Champagne & Glezer 1993; Yun, Kim & Choi 2006). However, it is worth noting that Johansson, George & Woodward (2002) reported the presence of a distinct very low-frequency mode, $St \to 0$, at azimuthal wavenumber $m = 2$ in their proper orthogonal decomposition (POD) analyses of the turbulent wake of a circular disk at $Re \approx 2.5 \times 10^4$. This mode is distinct from the VS mode of a circular disk wake, which resides at $m = 1$ with $St = 0.135$ (Berger *et al.* 1990). In a subsequent study, Johansson & George (2006) extended the downstream distance to $x/D = 150$ and found that the $m = 2$ mode with $St \to 0$ dominated the far wake of the disk in terms of energy content relative to the VS mode. This finding was corroborated in the SPOD analysis (Nidhan *et al.* 2020) of a disk wake at a higher Reynolds number ($Re = 5 \times 10^4$). The authors further found low-rank behaviour of the SPOD modes and that almost the entire Reynolds shear stress could be reconstructed with the leading SPOD modes of $m \leq 4$. Streamwise-elongated streaks, a focus of the current paper, were not considered by Nidhan *et al.* (2020).

None of the wake studies that report the presence and the eventual dominance at large x of the very low-frequency mode ($St \to 0$) at $m = 2$ explains the physical origins of this structure. To address this gap, we revisit the LES database of Chongsiripinyo & Sarkar (2020), who simulated the wake of a circular disk up to an unprecedented downstream distance of $x/D = 125$. The large streamwise domain enables us to investigate the entire wake. Unlike the previous SPOD analysis (Nidhan *et al.* 2020) of this wake database, we focus on the streaky structures. We attempt to answer the following questions. Can streaky structures be identified in the near and far fields of the turbulent wake? Is the lift-up mechanism active in the turbulent wake? How do the energetics and spatial structure of streaks evolve with downstream distance? What, if any, is the link between the streak and the well-documented and extensively studied VS mode?

In this work, besides visualizations and classical statistical analyses, we utilize two modal techniques, SPOD and bispectral mode decomposition (BMD), to shed light on the aforementioned questions. The SPOD technique, whose mathematical framework in the context of turbulent flow was laid out by Lumley (1967, 1970), extracts a set of orthogonal modes sorted according to their energy at each frequency. It distinguishes the different time scales of the flow and identifies the most energetic coherent structures at each time scale. The SPOD modes are coherent in both space and time, and represent the flow structures in a statistical sense (Towne, Schmidt & Colonius 2018). Early applications of SPOD were by Glauser, Leib & George (1987), Glauser & George (1992) and Delville (1994), and this method has regained popularity since the work by Towne *et al.* (2018) and Schmidt *et al.* (2018). This technique is particularly suitable for detecting and educing modes corresponding to streaky structures in statistically stationary flows (Nogueira *et al.*

2019; Abreu *et al.* 2020; Pickering *et al.* 2020), and is hence employed in this work. The BMD technique, proposed by Schmidt (2020), extracts the flow structures that are generated through triadic interactions. It identifies the most dominant triads in the flow by maximizing the spatially integrated bispectrum. Furthermore, it picks out the spatial regions of nonlinear interactions between the coherent structures. This technique has been used to characterize the triadic interactions in various flow configurations, such as laminar–turbulent transition on a flat plate (Goparaju & Gaitonde 2022), forced jets (Maia *et al.* 2021; Nekkanti *et al.* 2022, 2023), swirling flows (Moczarski *et al.* 2022) and wake of an aerofoil (Patel & Yeh 2023). In this work, we will employ BMD to investigate the presence and strength of nonlinear interactions between the VS mode and the streak-containing modes.

The paper is organized as follows. In § 2, the dataset and numerical methodology of SPOD and BMD are discussed. Section 3 presents the extraction and visualization of streaks and the lift-up mechanism in the near and far wakes. Results from SPOD analysis at different downstream locations are presented in § 4, with a particular emphasis again on streaks and the lift-up mechanism. Section 5 presents the results from the analysis of nonlinear interactions in the wake at select locations. The paper ends with discussion and conclusions in § 6.

2. Numerical wake database and methods for its analysis

2.1. *Dataset description*

The dataset employed for the present study of wake dynamics is from the high-resolution LES of flow past a circular disk at Reynolds number $Re = U_\infty D/\nu = 5 \times 10^4$, reported in Chongsiripinyo & Sarkar (2020). Here, U_∞ is the freestream velocity, D is the disk diameter, and ν is the kinematic viscosity. The case of a homogeneous fluid from Chongsiripinyo & Sarkar (2020), who also simulate stratified wakes, is selected here. The filtered Navier–Stokes equations, subject to the condition of solenoidal velocity, were solved numerically on a structured cylindrical grid that spans a radial distance $r/D = 15$ and a streamwise distance $x/D = 125$. An immersed boundary method (Balaras 2004) is used to represent the circular disk in the simulation domain, and the dynamic Smagorinsky model (Germano *et al.* 1991) is used for the LES model. The numbers of grid points in the radial (r), azimuthal (θ) and streamwise (x) directions are $N_r = 365$, $N_\theta = 256$ and $N_x = 4096$, respectively. The simulation has high resolution, with streamwise grid resolution $\Delta x = 10\eta$ at $x/D = 10$, where η is the Kolmogorov length scale. By $x/D = 125$, the resolution improves to $\Delta x < 6\eta$ so that the onus on the subgrid model decreases progressively. Readers are referred to Chongsiripinyo & Sarkar (2020) for a detailed description of the numerical methodology and grid quality.

2.2. *Spectral proper orthogonal decomposition*

The SPOD technique is the frequency-domain variant of POD. It computes monochromatic modes that are optimal in terms of the energy norm of the flow, e.g. TKE for the wake flow at hand. The SPOD modes are the eigenvectors of the cross-spectral density matrix, which is estimated using Welch's approach (Welch 1967). Here, we provide a brief overview of the method. For a detailed mathematical derivation and algorithmic implementation, readers are referred to Towne *et al.* (2018) and Schmidt & Colonius (2020).

For a statistically stationary flow, let $\boldsymbol{q}_i = \boldsymbol{q}(t_i)$ denote the mean subtracted snapshots, where $i = 1, 2, \ldots, n_t$ gives the number of snapshots. For spectral estimation, the dataset is first segmented into n_{blk} overlapping blocks, with n_{fft} snapshots in each block. The neighbouring blocks overlap by n_{ovlp} snapshots, with $n_{ovlp} = n_{fft}/2$. The n_{blk} blocks are then Fourier transformed in time, and all Fourier realizations of the lth frequency $\boldsymbol{q}_l^{(j)}$ are arranged in a matrix:

$$\hat{\boldsymbol{Q}}_l = \left[\hat{\boldsymbol{q}}_l^{(1)}, \hat{\boldsymbol{q}}_l^{(2)}, \ldots, \hat{\boldsymbol{q}}_l^{(n_{blk})}\right]. \tag{2.1}$$

The SPOD eigenvalues $\boldsymbol{\Lambda}_l$ are obtained by solving the eigenvalue problem

$$\frac{1}{n_{blk}} \hat{\boldsymbol{Q}}_l^* \boldsymbol{W} \hat{\boldsymbol{Q}}_l \boldsymbol{\Psi}_l = \boldsymbol{\Psi}_l \boldsymbol{\Lambda}_l, \tag{2.2}$$

where $\boldsymbol{W}$ is a positive-definite Hermitian matrix that accounts for the component-wise and numerical quadrature weights, and $(\cdot)^*$ denotes the complex conjugate. The SPOD modes at the lth frequency are recovered as

$$\boldsymbol{\Phi}_l = \frac{1}{\sqrt{n_{blk}}} \hat{\boldsymbol{Q}}_l \boldsymbol{\Psi}_l \boldsymbol{\Lambda}_l^{-1/2}. \tag{2.3}$$

The SPOD eigenvalues are denoted by $\boldsymbol{\Lambda}_l = \mathrm{diag}\left(\lambda_l^{(1)}, \lambda_l^{(2)}, \ldots, \lambda_l^{(n_{blk})}\right)$. By construction, $\lambda_l^{(1)} \geq \lambda_l^{(2)} \geq \cdots \geq \lambda_l^{(n_{blk})}$ represent the energies of the corresponding SPOD modes that are given by the column vectors of the matrix $\boldsymbol{\Phi}_l = \left[\boldsymbol{\phi}_l^{(1)}, \boldsymbol{\phi}_l^{(2)}, \ldots, \boldsymbol{\phi}_l^{(n_{blk})}\right]$. The SPOD mode $\boldsymbol{\phi}_l^{(j)}$ represents the jth dominant coherent flow structure at the lth frequency. An useful property of the SPOD modes is their orthogonality; the weighted inner product at each frequency is $\langle \boldsymbol{\phi}_l^{(i)}, \boldsymbol{\phi}_l^{(j)} \rangle = (\boldsymbol{\phi}_l^{(i)})^* \boldsymbol{W} \boldsymbol{\phi}_l^{(j)} = \delta_{ij}$.

Here, we perform SPOD on various two-dimensional streamwise planes ranging from $x/D = 1$ to $x/D = 120$. Thus $\boldsymbol{q}$ contains the three velocity components at the discretized grid nodes on a streamwise-constant plane. These planes are sampled at spacing $5D$ from $x/D = 5$ to $x/D = 100$, and five additional planes are sampled at $x/D = 1, 2, 3, 110, 120$. The utilized time series has $n_t = 7200$ snapshots, with uniform separation of non-dimensional time $\Delta t U_\infty/D = 0.072$ between two snapshots. Owing to the periodicity in the azimuthal direction, the flow field is first decomposed into azimuthal wavenumbers m,

$$q(x, r, \theta, t) = \sum_m \hat{q}_m(x, r, t), \tag{2.4}$$

and then SPOD is applied on the data at each azimuthal wavenumber. The spectral estimation parameters used here are $n_{fft} = 512$ and $n_{ovlp} = 256$, resulting in $n_{blk} = 27$ SPOD modes for each St. Each block used for the temporal fast Fourier transform spans a time duration $\Delta T = 36.91 U_\infty/D$.

2.3. *Reconstruction using convolution approach*

The convolution strategy proposed by Nekkanti & Schmidt (2021) is employed for low-dimensional reconstruction of the flow field. This involves computing the expansion

coefficients by convolving the SPOD modes over the data one snapshot at a time:

$$a_l^{(i)}(t) = \int_{\Delta T}\int_{\Omega} (\boldsymbol{\phi}_l^{(i)}(x))^* \, \boldsymbol{W}(x)\, \boldsymbol{q}(x, t+\tau)\, w(\tau)\, \mathrm{e}^{-\mathrm{i}2\pi f_l \tau}\, \mathrm{d}x\, \mathrm{d}\tau. \tag{2.5}$$

Here, $w(\tau)$ is the Hamming windowing function, and Ω is the spatial domain of interest. The data at time t are then reconstructed as

$$\boldsymbol{q}(t) \approx \sum_l \sum_i a_l^{(i)}(t)\, \boldsymbol{\phi}_l^{(i)}\, \mathrm{e}^{-\mathrm{i}2\pi f_l t}. \tag{2.6}$$

2.4. *Bispectral mode decomposition*

Bispectral mode decomposition (BMD) is a technique proposed recently by Schmidt (2020) to characterize the coherent structures associated with triadic interactions in statistically stationary flows. Here, we provide a brief overview of the method. The reader is referred to Schmidt (2020) for further details of the derivation and mathematical properties of the method.

The BMD technique is an extension of classical bispectral analysis to multidimensional data. The classical bispectrum is defined as the double Fourier transform of the third moment of a time signal. For a time series $y(t)$ with zero mean, the bispectrum is

$$S_{yyy}(f_1, f_2) = \iint R_{yyy}(\tau_1, \tau_2)\, \mathrm{e}^{-\mathrm{i}2\pi(f_1\tau_1 + f_2\tau_2)}\, \mathrm{d}\tau_1\, \mathrm{d}\tau_2, \tag{2.7}$$

where $R_{yyy}(\tau_1, \tau_2) = E[y(t)\, y(t-\tau_1)\, y(t-\tau_2)]$ is the third moment of $y(t)$, and $E[\cdot]$ is the expectation operator. The bispectrum is a signal processing tool for one-dimensional time series that measures the quadratic phase coupling only at a single spatial point. In contrast, BMD identifies the intensity of the triadic interactions over the spatial domain of interest, and extracts the corresponding spatially coherent structures.

Also, BMD maximizes the spatial integral of the pointwise bispectrum:

$$b(f_k, f_l) = E\left[\int_{\Omega} \hat{\boldsymbol{q}}^*(x, f_k) \circ \hat{\boldsymbol{q}}^*(x, f_l) \circ \hat{\boldsymbol{q}}(x, f_k + f_l)\, \mathrm{d}x\right]. \tag{2.8}$$

Here, $\hat{\boldsymbol{q}}$ is the temporal Fourier transform of $\boldsymbol{q}$ computed using the Welch (1967) approach, and $\circ$ denotes the Hadamard (or elementwise) product.

Next, as in (2.1), all the Fourier realizations at the lth frequency are arranged into the matrix $\hat{\boldsymbol{Q}}_l$. The auto-bispectral matrix is then computed as

$$\boldsymbol{B} = \frac{1}{n_{blk}}\, \hat{\boldsymbol{Q}}_{k\circ l}^H \boldsymbol{W} \hat{\boldsymbol{Q}}_{k+l}, \tag{2.9}$$

where $\hat{\boldsymbol{Q}}_{k\circ l}^H = \hat{\boldsymbol{Q}}_k^* \circ \hat{\boldsymbol{Q}}_l^*$.

To measure the interactions between different quantities, we construct the cross-bispectral matrix

$$\boldsymbol{B}_c = \frac{1}{n_{blk}}\, (\hat{\boldsymbol{Q}}_k^* \circ \hat{\boldsymbol{R}}_l^*) \boldsymbol{W} \hat{\boldsymbol{S}}_{k+l}. \tag{2.10}$$

In the present application, matrices $\boldsymbol{Q}$, $\boldsymbol{R}$ and $\boldsymbol{S}$ comprise the time series of the field variables at the azimuthal wavenumber triad $[m_1, m_2, m_3]$.

Owing to the non-Hermitian nature of the bispectral matrix, the optimal expansion coefficients $\boldsymbol{a}_1$ are obtained by maximizing the absolute value of the Rayleigh quotient of $\boldsymbol{B}$ (or $\boldsymbol{B}_c$):

$$\boldsymbol{a}_1 = \arg\max_{\|\boldsymbol{a}\|=1} \left| \frac{\boldsymbol{a}^* \boldsymbol{B} \boldsymbol{a}}{\boldsymbol{a}^* \boldsymbol{a}} \right|. \tag{2.11}$$

The complex mode bispectrum is then obtained as

$$\lambda_1(f_k, f_l) = \left| \frac{\boldsymbol{a}_1^* \boldsymbol{B} \boldsymbol{a}_1}{\boldsymbol{a}_1^* \boldsymbol{a}_1} \right|. \tag{2.12}$$

Finally, the leading-order bispectral modes and the cross-frequency fields are recovered as

$$\boldsymbol{\phi}_{k+l}^{(1)} = \hat{\boldsymbol{Q}}_{k+l} \boldsymbol{a}_1 \tag{2.13}$$

and

$$\boldsymbol{\phi}_{k\circ l}^{(1)} = \hat{\boldsymbol{Q}}_{k\circ l} \boldsymbol{a}_1, \tag{2.14}$$

respectively. By construction, the bispectral modes and cross-frequency fields have the same set of expansion coefficients. This ensures explicitly the causal relation between the resonant frequency triad $(f_k, f_l, f_k + f_l)$, where $\hat{\boldsymbol{Q}}_{k\circ l}$ is the cause, and $\hat{\boldsymbol{Q}}_{k+l}$ is the effect. The complex mode bispectrum λ_1 measures the intensity of the triadic interaction, and the bispectral mode $\boldsymbol{\phi}_{k+l}$ represents the structures that result from the nonlinear triadic interaction.

Similar to SPOD, we perform BMD on various two-dimensional streamwise planes and use the same spectral estimation parameters $n_{fft} = 512$ and $n_{ovlp} = 256$. Since our focus is on interactions of different azimuthal wavenumbers, the cross-BMD method, which computes the cross-bispectral matrix $\boldsymbol{B}_c$, is applied to the wake database. The specific interactions among different m and their analysis using BMD will be presented and discussed in § 5.1.

3. Flow structures

3.1. *Streaky structures in the near and far wake*

Nidhan *et al.* (2020) showed that the near and far fields of the wake of a circular disk are dominated by two distinct modes, residing at (i) $m = 1$, $St = 0.135$, and (ii) $m = 2$, $St \to 0$. While the former mode is the VS mode in the wake of a circular disk (Fuchs, Mercker & Michel 1979*a*; Berger *et al.* 1990; Cannon *et al.* 1993), the physical origin of the latter mode remains unclear. Johansson & George (2006) hint that the $m = 2$ mode is linked to 'very' large-scale features that twist the mean flow slowly. Motivated by the findings of Nidhan *et al.* (2020) and the discussion in Johansson & George (2006), we investigate the streamwise manifestation of the azimuthal modes $m = 1$ and $m = 2$. The main result is that, different from the $m = 1$ mode, the $m = 2$ mode is associated with streamwise-aligned streaky structures.

Figure 1 shows the azimuthal modes $m = 1$ and $m = 2$ of an instantaneous flow snapshot in the wake spanning downstream distance $0 < x/D < 100$, obtained using a Fourier transform in the azimuthal direction θ. In the $m = 1$ mode (figure 1*a*), a wavelength $\lambda/D = 1/St_{VS}$ (where the VS frequency is $St_{VS} \approx 0.13$–0.14) is evident throughout the domain. This observation is in agreement with previous studies (Johansson *et al.* 2002;

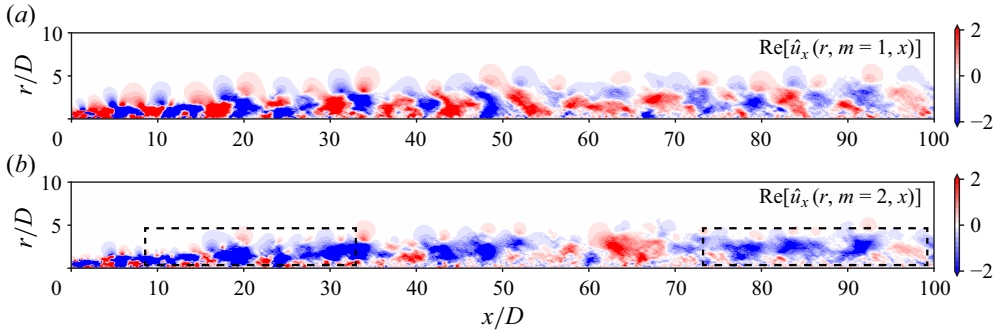

Figure 1. Azimuthally decomposed instantaneous fields of the streamwise velocity (u_x) for (a) $m = 1$ and (b) $m = 2$ azimuthal modes. Rectangular boxes in (b) show large-scale streaks in the $m = 2$ field.

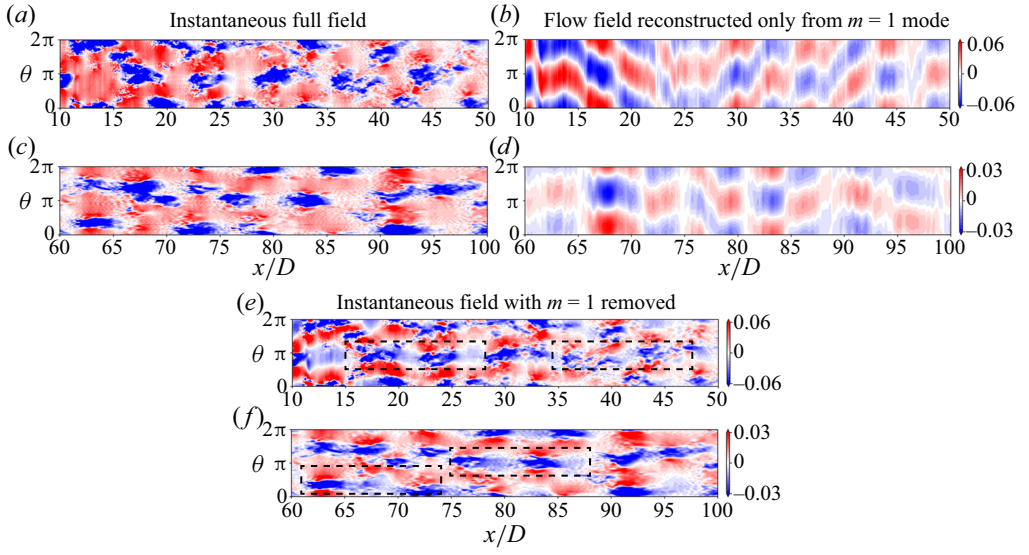

Figure 2. Instantaneous streamwise velocity on x/D–θ planes at (a,b,e) $r/D = 1.25$ and (c,d,f) $r/D = 2.5$. Plots (a,c) show the full streamwise velocity field; (b,d) show the field reconstructed from the $m = 1$ contribution only; (e,f) show the field with the $m = 1$ contribution removed. Rectangular boxes in (e,f) emphasize the large-scale streaks in the flow field with the $m = 1$ mode removed.

Johansson & George 2006; Nidhan *et al.* 2020) that report the existence of the VS mode at significantly large downstream locations $\sim O(100D)$ from the disk.

The spatial structure of the $m = 2$ mode (figure 1b) is quite different from that of the $m = 1$ mode. In the $m = 2$ mode visualization, distinct elongated structures are present throughout the domain. Notice in particular the structures inside the dashed rectangular boxes. The streamwise extent of these structures can be up to $\lambda_x/D \approx 25$ (see $70 < x/D < 95$), significantly larger than the wavelength of the VS mode $\lambda_x/D \approx 7$.

Figures 2(a,c) show the instantaneous streamwise velocity field in the near–intermediate and intermediate–far wakes, respectively, of the disk on a x/D–θ plane. The x/D–θ plane is constructed by unrolling the cylindrical surface at a constant r/D. For the near–intermediate field (figure 2a), the plane is located at $r/D = 1.25$, while for the intermediate–far field (figure 2c), $r/D = 2.5$ is chosen. In both figures, VS structures are evident, spaced at an approximate wavelength $\lambda_x/D \approx 7$. These structures and the

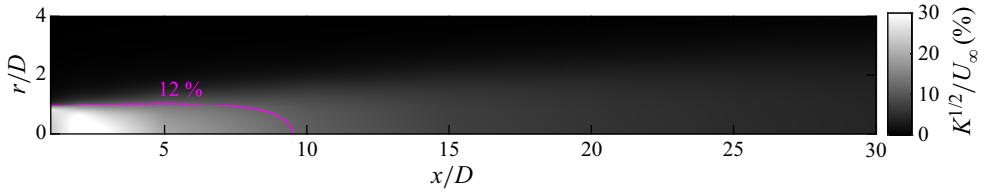

Figure 3. Turbulence intensity ($K^{1/2}/U_\infty$) as a function of streamwise (x) and radial (r) directions. The magenta curve demarcates the region where $K^{1/2}/U_\infty$ reduces to 0.12.

wavelength $\lambda_x/D \approx 7$ become even more evident when the flow fields at the respective radial locations in the near–intermediate and intermediate–far wakes are constructed with only the $m = 1$ mode, as shown in figures 2(*b*,*d*). Upon removing the contribution of the VS mode that lies in the $m = 1$ azimuthal wavenumber (Johansson *et al.* 2002; Johansson & George 2006; Nidhan *et al.* 2020), the streaks become readily apparent in figures 2(*b*,*d*). See again the structures contained inside dashed rectangular boxes in figures 2(*e*,*f*). These observations in figures 1 and 2 are strong initial indications of the presence of large-scale streaks in turbulent wakes, similar to those reported recently in the numerical and experimental datasets of turbulent jets (Nogueira *et al.* 2019; Pickering *et al.* 2020). In what follows, the characteristics and robustness of these elongated structures are quantified through various statistical and spectral measures.

To this end, we invoke Taylor's hypothesis, converting time t at a location x_0 to pseudo-streamwise distance from x_0: $x_t = U_{conv}t$, where $U_{conv} = U_\infty - U_d$ is the convective velocity. Since the defect velocity in the wake is $U_d \ll U_\infty$ (where U_∞ is the freestream velocity), U_{conv} is approximated by U_∞. Taylor's hypothesis requires velocity fluctuation to be sufficiently small compared to U_{conv}. Figure 3 shows that this requirement is met since turbulence intensity ($K^{1/2}/U_\infty$) drops below 12 % beyond $x/D = 10$ for all radial locations, and below 4 % at $x/D = 30$. Previous work on turbulent wakes has shown Taylor's hypothesis to be valid in the wake when $K^{1/2}/U_\infty$ drops below ∼10 % (Antonia & Mi 1998; Kang & Meneveau 2002; Dairay, Obligado & Vassilicos 2015; Obligado, Dairay & Vassilicos 2016). Invoking Taylor's hypothesis gives $St \approx U_\infty k_x$. In this study, we will focus particularly on $St \to 0$ (obtained from either temporal spectra or SPOD at different x/D locations), which, by Taylor's hypothesis, is equivalent to large-scale streaks with $k_x \to 0$ (k_x being the streamwise wavenumber) at those locations.

The near-to-intermediate wake behaviour is shown at $x_0/D = 10$ in figures 4(*a*,*c*,*e*), and at $x_0/D = 20$ in figures 4(*b*,*d*,*f*), through plots of streamwise velocity fluctuation (u'_x) at $r/D = 0.8$ in the x_t/D–θ plane. Time t is transformed to the x_t coordinate by application of Taylor's hypothesis, which is valid beyond $x/D \geq 9$ in the wake, as was shown through figure 3 and the associated discussion.

Due to the strong signature of the VS mode in the near-to-intermediate wake, alternate patches of inclined positive and negative fluctuations separated by $\lambda_D \approx 1/St_{VS}$ dominate the visualization in figures 4(*a*,*b*). It is known *a priori* that these structures are contained in the $m = 1$ azimuthal mode. In order to assess space-time coherence other than the VS mode, the streamwise fluctuations are replotted in figures 4(*c*,*d*) after removing the $m = 1$ contribution. Once the $m = 1$ contribution is removed, streamwise streaks become evident at both locations. Furthermore, one can also observe that these streaks appear to be contained primarily in the azimuthal mode $m = 2$, i.e. there are two structures over the azimuthal length of 2π. Only the $m = 2$ component is shown in figures 4(*e*,*f*),

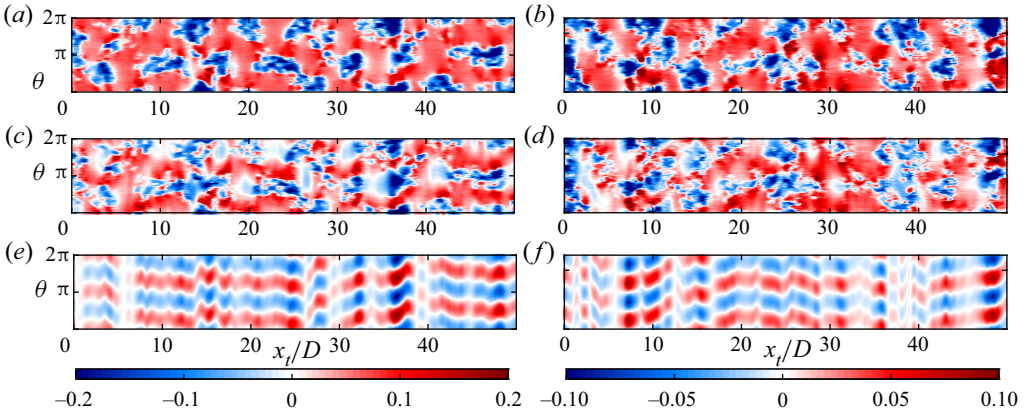

Figure 4. Streamwise velocity fluctuations u_x' on an x_t/D–θ plane at $r/D \approx 0.8$, for (a,c,e) $x_0/D = 10$, and (b,d,f) $x_0/D = 20$. Plots (a,b) include all azimuthal components; (c,d) exclude $m = 1$; and (e,f) include solely $m = 2$.

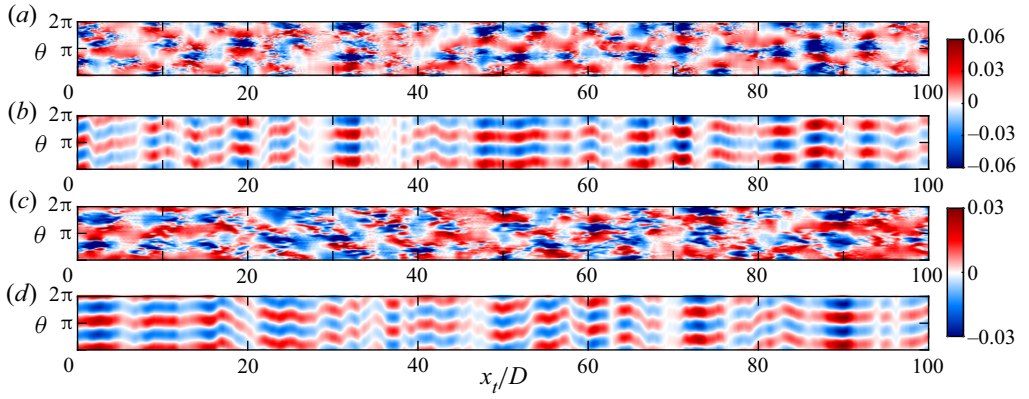

Figure 5. The u_x' field on a x_t/D–θ plane at $r/D \approx 2.0$, for (a,b) $x_0/D = 40$, and (c,d) $x_0/D = 80$. In (a,c), $m = 1$ is removed, and in (b,d), only $m = 2$ is shown.

where the elongated streamwise streaks come into sharper focus. Building upon figure 1, figures 4(c–f) lend support to the spatiotemporal robustness of these large-scale streaks in the turbulent wake of circular disk.

The downstream distance ($0 < x/D < 120$) spanned in the simulations of Chongsiripinyo & Sarkar (2020) is very large, thus enabling the far field to be probed too for the presence (or absence) of the streamwise streaks. Figures 5(a,c) show the x_t/D–θ plots of u_x', with the contribution of the $m = 1$ mode excluded, in regions starting at $x_0/D = 40$ and 80. The x_t/D–θ planes are located at $r/D = 2$ for these far-wake locations since the wake width grows with x. Interested readers can refer to figures 5, 15 and 16 of Chongsiripinyo & Sarkar (2020), and figure 5 of Nidhan *et al.* (2020), for an in-depth discussion about the mean and turbulence statistics. Similar to the near-wake plot in figures 4(c,d), large-scale streaks elongated in the streamwise direction are found to extend into the far wake as well. Once again, isolating the $m = 2$ component (figures 5b,d) highlights the streaks. Collectively, figures 4 and 5 demonstrate that the streaks span the entire wake length and that the $m = 2$ mode drives these streaks.

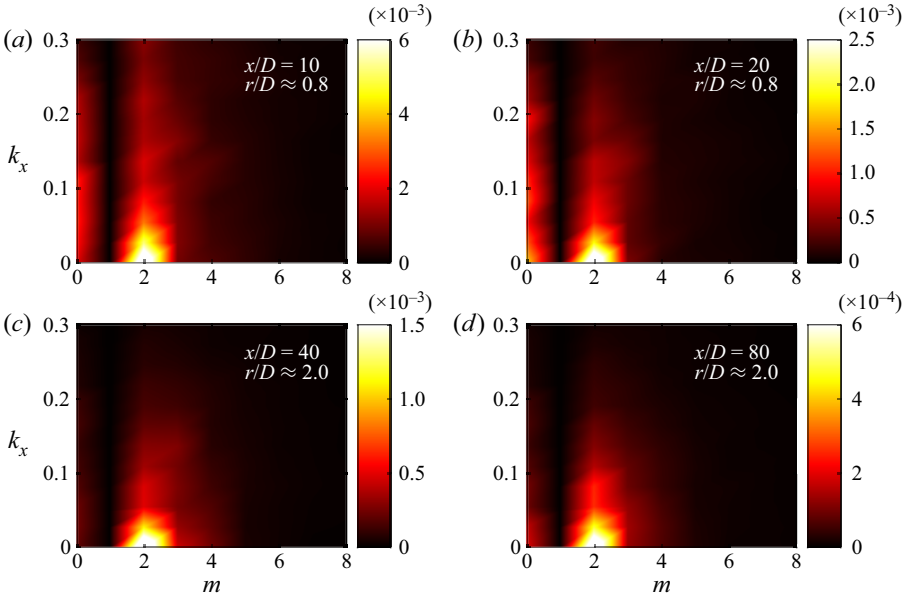

Figure 6. Two-dimensional power spectral density of the streamwise velocity fluctuation in k_x–m space, for: (*a*) $x/D = 10$, $r/D \approx 0.8$; (*b*) $x/D = 20$, $r/D \approx 0.8$; (*c*) $x/D = 40$, $r/D \approx 2.0$; (*d*) $x/D = 80$, $r/D \approx 2.0$. The $m = 1$ wavenumber is removed so as to de-emphasize the VS structure.

Figure 6 shows two-dimensional spectra in the streamwise wavelength versus azimuthal mode (k_x–m) space at four representative streamwise locations, $x/D = 10$, 20, 40 and 80. Here, k_x is the wavenumber of the pseudo-streamwise direction x_t. The $m = 1$ contribution is removed *a priori* to emphasize the large-scale streaks. At all these four locations, these streaky structures correspond to $k_x \to 0$ and are found to reside in the $m = 2$ azimuthal mode. Note that $k_x = 0$, $St = 0$ should be interpreted as k_x, $St \to 0$ as the length of the time series is not sufficient to resolve the large time scale of streaks. In Appendix A, we vary the spectral estimation parameter n_{fft} to resolve the lower frequencies and identify the frequency associated with streaks in this limit to be $St \approx 0.006$.

3.2. *Evidence of lift-up mechanism in the wake*

Previous work in turbulent free shear flows and wall-bounded flows often attributes the formation of streaks in the velocity to the lift-up mechanism (Ellingsen & Palm 1975; Landahl 1975). The lift-up mechanism, by sweeping fluid from high-speed regions to low-speed regions, and vice versa, leads to the formation of high-speed and low-speed streaks, respectively. Brandt (2014) provides a comprehensive review of the lift-up mechanism and its crucial role in various fundamental phenomena, e.g. subcritical transition in shear flows, self-sustaining cycle in wall bounded flows, and disturbance growth in complex flows.

To investigate the presence of the lift-up mechanism in the wake, we plot conditional averages of streamwise vorticity fluctuations (ω_x) at three representative locations in the flow – the planes $x/D = 10$, 40 and 80 in figure 7. Figures 7(*a*,*b*,*c*) show a conditional average $\langle \omega_x^{c1} \rangle$ designed to extract the structure of the streamwise vorticity on a constant-x plane during times of large streamwise velocity fluctuations. Specifically, the condition

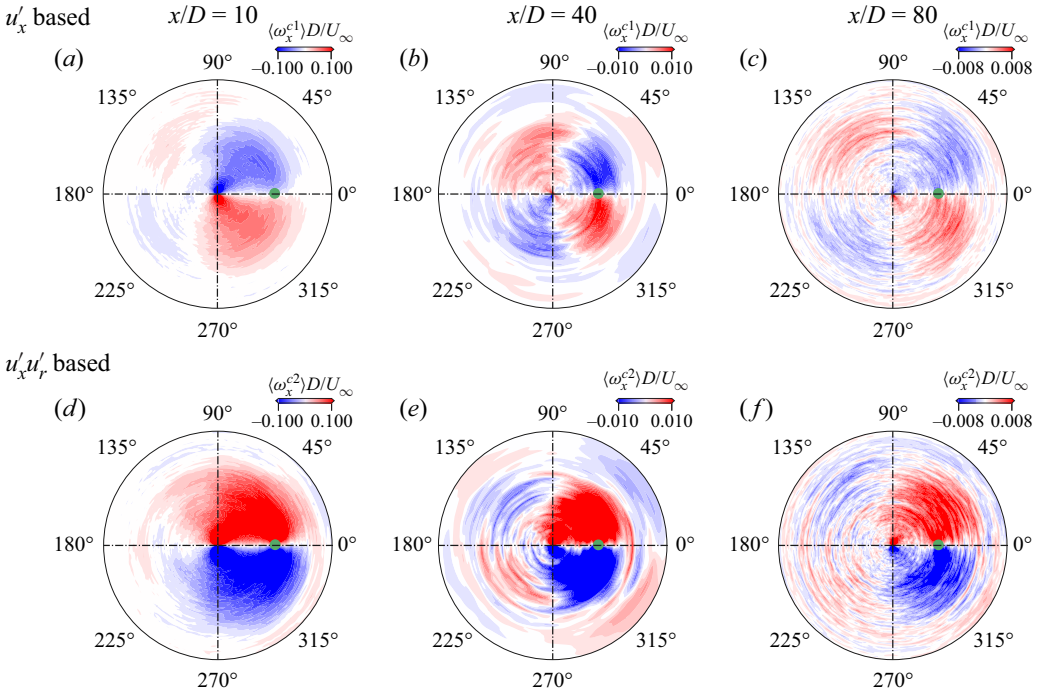

Figure 7. Conditionally-averaged streamwise vorticity at (a,d) $x/D = 10$, (b,e) $x/D = 40$, and (c,f) $x/D = 80$. Plots (a,b,c) show $\langle\omega_x^{c1}\rangle$, conditioned using u'_x, and (d,e,f) show $\langle\omega_x^{c2}\rangle$, conditioned using $u'_x u'_r$. The green dot shows the location of the conditioning point: (a,d) $r/D \approx 0.8$, $\theta \approx 0°$, and (b,c,e,f) $r/D \approx 2$, $\theta \approx 0°$. The radial domain extends until $r/D = 2$ at $x/D = 10$, and until $r/D = 5$ at $x/D = 40, 80$. Positive vorticity (red) is out of the plane, and negative vorticity (blue) is into the plane.

is that

$$u'_x \geq c(u'_x)^{rms} \tag{3.1}$$

at a specified point P on that plane, and $\langle\omega_x^{c1}\rangle$ is the temporal average of all $\omega_x(t)$ that satisfy this condition. The conditional point P (shown as green dots in figure 7) is chosen to lie at $\theta = 0$ and radial locations $r/D = 0.8$ and 2 for $x/D = 10$ and $x/D = 40, 80$, respectively. The selection of different radial locations at $x/D = 10$ and $x/D = 40, 80$ is based on the approximate values of mean wake half-widths at the respective x/D locations (Chongsiripinyo & Sarkar 2020). Owing to rotational invariance of statistics for an axisymmetric wake, the condition is applied to a new point P_1 at the same r/D but a different value of θ, and the new $\langle\omega_x^{c1}\rangle$ field, after a rotation to bring P_1 to P, is included in the conditional average. Since $N_\theta = 256$ points are used for discretization, the ensemble used for the conditional average is expanded significantly by exploiting rotational invariance of statistics. Figures 7(d,e,f) show $\langle\omega_x^{c2}\rangle$ computed using a different condition at point P,

$$-u'_x u'_r \geq c(-u'_x u'_r)^{rms}. \tag{3.2}$$

This condition is designed to identify the structure of streamwise vorticity at times of significant Reynolds shear stress at point P. The results exhibit moderate sensitivity to $c \in (0, 1]$, as reported in Appendix B. Hence c is set to 0.5 as a compromise between identification of intense events and retention of sufficient snapshots for conditional averaging. Here, $(u'_x)^{rms}$ and $(-u'_x u'_r)^{rms}$ are the root-mean-square (r.m.s.) values of the

streamwise velocity fluctuations and the r.m.s. values of the streamwise–radial fluctuations correlation at the conditioning points, respectively.

The conditionally averaged field based on (3.1) captures the structure of the streamwise vorticity field during events of intense positive u'_x. In figure 7(a), two rolls of streamwise vorticity are observed in the conditionally averaged field: negative on the top and positive at the bottom of the conditioning point, respectively. These streamwise vortex rolls push the high-speed fluid in the outer wake to the low-speed region in the inner wake around the conditioning points (green dot), leading to $u'_x > 0$. When the averaging procedure is conditioned on negative streamwise velocity fluctuations, i.e. $u'_x \leq -c(u'_x)^{rms}$, the signs of the vortex rolls in figure 7 are interchanged, as expected (not shown). At $x/D = 40$ and 80 (figures 7b,c), two additional vortical structures are observed in the $\theta = [90°, 270°]$ region. However, around the conditioning point, the spatial organization of vorticity remains qualitatively similar. The size of these vortex rolls increases with x/D, consistent with the radial spread of the wake.

The conditionally averaged field based on (3.2) captures the vorticity field corresponding to intense positive $-u'_x u'_r$ values. In a turbulent wake, $-u'_x u'_r$ is predominantly positive such that the dominant production term in the wake, $P_{xr} = \langle -u'_x u'_r \rangle \, \partial U/\partial r > 0$, acts to transfer energy from the mean flow to turbulence. Now turning to (3.2), positive $-u'_x u'_r$ can result from two scenarios: (i) $u'_r > 0$, $u'_x < 0$, i.e. 'ejection' of low-speed fluid from the inner wake to the outer wake; and (ii) $u'_r < 0$, $u'_x > 0$, i.e. 'sweep' of high-speed fluid from outer wake to inner wake. Both of the above-mentioned scenarios are consistent with the lift-up mechanism. If ejection and sweep events were equally probable, then $\langle \omega_x^{c2} \rangle \approx 0$ due to the opposite spatial distribution of vortices during ejection and sweep events. However, $\langle \omega_x^{c2} \rangle$ obtained from $-u'_x u'_r$ based conditioning (figures 7d,e,f) shows that the positive and negative vortices are spatially organized such that the flow induced by these vortices at the conditioning point is outwards ($u'_r > 0$), pushing low-speed fluid from the inner wake to the outer wake. In short, $\langle \omega_x^{c2} \rangle$ fields in figures 7(d,e,f) correspond to the ejection events at the conditioning point. A similar spatial organization of $\langle \omega_x^{c2} \rangle$ is observed across the wake cross-section when the radial location of the conditioning point is varied (plots not shown for brevity). This observation establishes that ejections are the dominant contributors to intense positive $-u'_x u'_r$, as opposed to sweep events, therefore ejections are more instrumental in the energy transfer from mean to turbulence. Previous studies (Kline *et al.* 1967; Corino & Brodkey 1969; Wallace 2016) of the turbulent boundary layer have also reported that ejection events are the primary contributors to Reynolds shear stress.

Figure 7 has two important implications. First, figures 7(a,b,c) demonstrate strong correlation between intense u'_x fluctuations and distinct streamwise vortical structures, indicating that the lift-up mechanism is active in the turbulent wake, in both the near field and the far field. Second, the conditionally averaged fields obtained using $u'_x u'_r$ inform us that the lift-up mechanism corresponding to the ejection of low-speed fluid from the inner wake to the outer wake is more dominant than the sweep of high-speed fluid from the outer wake to the inner wake. To the best of the authors' knowledge, both these observations constitute the first numerical evidence in the near and far fields of a canonical bluff body turbulent wake of (i) the lift-up mechanism, and (ii) the dominance of ejection events.

4. SPOD analysis of streaks in the wake

Section 3 reveals the presence of large-scale streaks and also that the lift-up mechanism is active in the wake. Furthermore, the $m = 2$ azimuthal wavenumber appears visually to

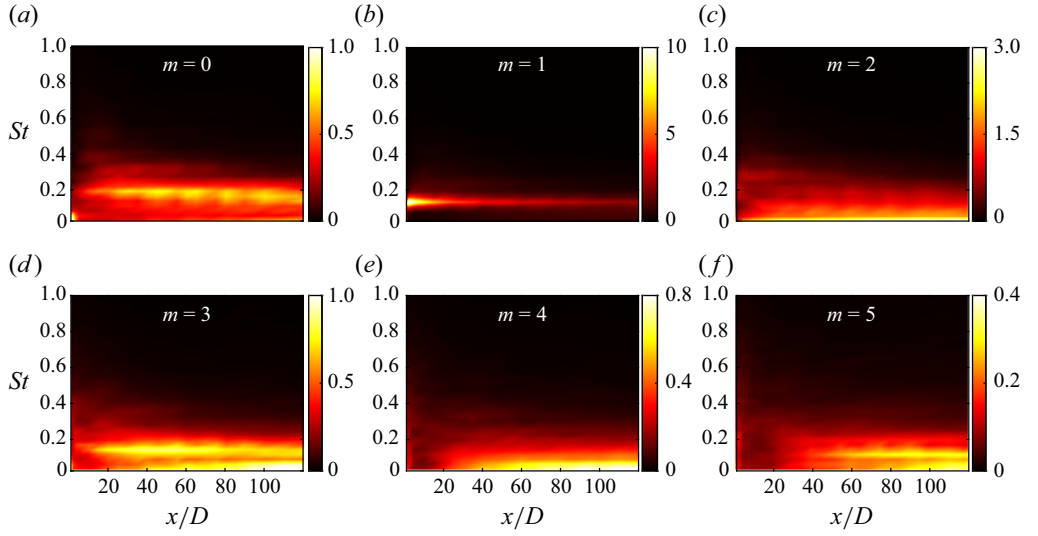

Figure 8. Percentage of energy contained in the leading SPOD modes $\lambda^{(1)}$ as a function of frequency St and streamwise location x/D at different azimuthal wavenumbers: (*a*) $m = 0$, (*b*) $m = 1$, (*c*) $m = 2$, (*d*) $m = 3$, (*e*) $m = 4$, and (*f*) $m = 5$. The leading SPOD eigenvalue $\lambda^{(1)}(St, x/D)$ is normalized with the total TKE $E_k^T(x/D)$ at the corresponding streamwise location, to calculate the percentage contribution.

be the dominant streak-containing mode. In this section, SPOD is employed to quantify the energetics and educe the dominant structures of the dominant features at $St \to 0$ in the wake. We focus particularly on the $m = 2$ mode, providing further evidence that these modes exhibit properties of streaks and are formed due to the lift-up mechanism. Direct comparison with the VS mode ($m = 1$, $St = 0.135$) is provided as appropriate to differentiate the role of streaks from that of the VS mode.

4.1. *Energetics of streaky structures using SPOD analysis*

The SPOD analysis is performed at different streamwise locations (x/D) in $1 \leq x/D \leq 120$. By definition, the leading SPOD mode at a given x/D represents the most energetic coherent structures at the associated frequency (St) and azimuthal wavenumber (m). Figure 8 shows the percentage of energy in the leading SPOD modes ($\lambda^{(1)}$) as a function of frequency and streamwise distance for the first six azimuthal wavenumbers, $m = 0$ to $m = 5$. The percentage of energy at each streamwise location is obtained by normalizing the leading eigenvalue with the total TKE, $E_k^T(x/D)$, at the corresponding location. Overall, the most significant contributors to the TKE are the VS mode ($m = 1, St = 0.135$) and the mode corresponding to streaks ($m = 2$, $St \to 0$), as reported in Nidhan *et al.* (2020). The leading VS SPOD mode contains about 10 % energy in the near-wake region ($5 \lesssim x/D \lesssim 15$) and decreases thereafter. The leading SPOD mode corresponding to the streaks in the $m = 2$ mode contains approximately 3 % energy from $x/D = 10$ onwards. The axisymmetric component ($m = 0$) exhibits a peak at $St \to 0.054$ at $x/D = 1$, and a much smaller peak at $St \approx 0.19$ for $10 \lesssim x \lesssim 120$. The former is associated with the pumping of the recirculation bubble (Berger *et al.* 1990), whereas the latter was observed in previous studies (see figure 12 in Berger *et al.* (1990), and figure 7 in Fuchs, Mercker & Michel (1979*b*)) but was not investigated further. The $m = 0$ mode is not the focus of this study.

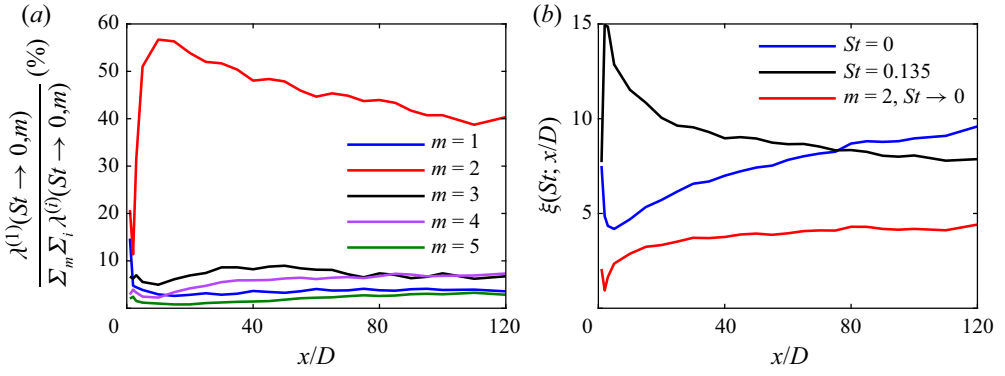

Figure 9. (*a*) Contributions of the leading SPOD modes $\lambda^{(1)}$ at different azimuthal wavenumbers to $St \to 0$. (*b*) Percentage energy contained in the frequencies $St = 0.135$ and $St \to 0$.

The energy $\lambda^{(1)}$ contained in the higher azimuthal wavenumbers ($m = 3$–5) is shown in figures 8(*d–f*), respectively. Although $\lambda^{(1)}$ is smaller than at $m = 1$ or $m = 2$, the higher modes also exhibit temporal structure. The $m = 3$ component shows energy concentration at the VS frequency $St = 0.135$ for $15 \lesssim x/D \lesssim 70$, and at $St \to 0$ for $x/D \gtrsim 50$. For $m = 4$, energy is concentrated near $St \to 0$ for $x/D \gtrsim 60$. For the $m = 5$ component, traces of the VS mode and streaks ($St \to 0$) are observed at the streamwise locations $x/D \gtrsim 60$ and $x/D \gtrsim 80$, respectively. Figure 8 indicates that the peaks at the VS frequency are present only at the odd azimuthal wavenumbers ($m = 1, 3, 5$), whereas the peaks corresponding to the large-scale streaks, i.e. $St \to 0$, can be found at both odd and even m. It is also interesting to note that for higher m, both the VS modes and streaks do not appear until larger values of x/D. This suggests nonlinear interactions among different frequencies and azimuthal wavenumbers as the wake evolves, as will be elaborated in § 5.

The $St \to 0$ streaks are dominated by the $m = 2$ azimuthal wavenumber, as demonstrated by figure 9(*a*), which shows the contribution of different m at $St \to 0$. The leading eigenvalues of each azimuthal wavenumber are normalized by the total energy at $St \to 0$, i.e. $\sum_m \sum_i \lambda^{(i)}(St \to 0, m)$. Streaks are azimuthally non-uniform structures and are not present in the axisymmetric $m = 0$ component. Hence we focus on $m \geq 1$. The azimuthal wavenumber $m = 2$ is energetically dominant at the $St \to 0$ frequency, containing about 40–50 % of the total energy at $St \to 0$. The suboptimal wavenumber is $m = 3$ for $5 \leq x \leq 80$, and switches between $m = 3$ and $m = 4$ thereafter. However, the difference in energy between the $m = 2$ and $m = 3$ wavenumbers is always large, >30 %. This dominance of the $m = 2$ wavenumber at $St \to 0$ is also consistent with the visualizations of the streamwise velocity fluctuations in figures 4 and 5, where one can see the presence of $m = 2$ even with the naked eye.

The energetic contribution of the two dominant frequencies, $St = 0.135$ (VS) and $St \to 0$ (streaks), is compared by computing the percentage of total energy (across all m and i) at a given frequency St as

$$\xi(St; x/D) = \frac{\sum_m \sum_i \lambda^{(i)}(m, St; x/D)}{E_k^T(x/D)} \times 100. \tag{4.1}$$

Figure 9(*b*) shows that the VS frequency is more dominant in the region $x \leq 70$, whereas the zeroth frequency dominates for $x \geq 70$. This implies that although the streaks are

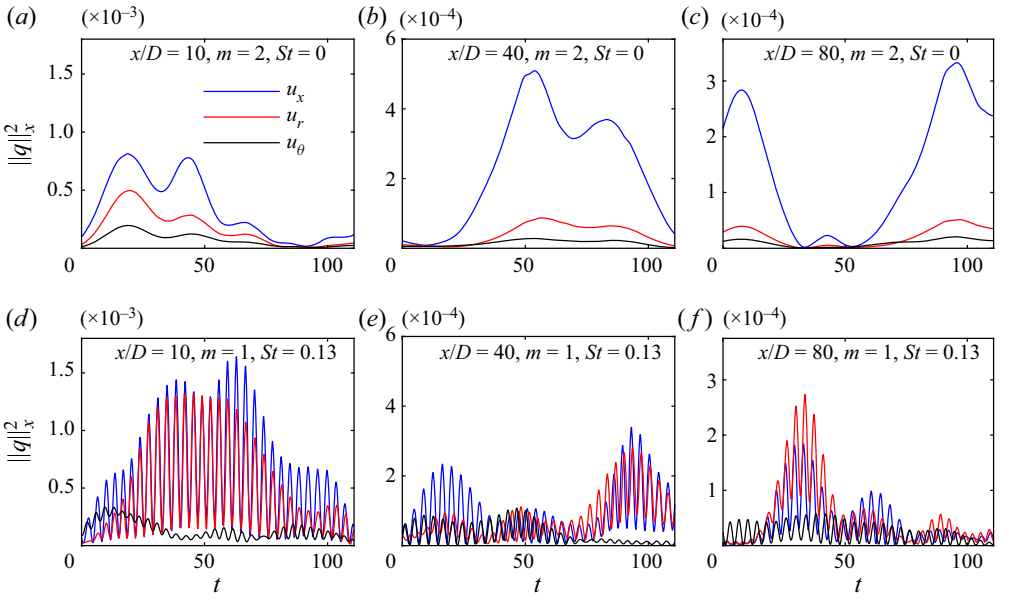

Figure 10. Component-wise instantaneous energy reconstructed from (*a–c*) the $m = 2$ streaky structures, and (*d–f*) the VS structures. The plane integral of the energy is shown at various streamwise locations: (*a*,*d*) $x/D = 10$, (*b*,*e*) $x/D = 40$, and (*c*,*f*) $x/D = 80$. Flow reconstruction uses the leading five SPOD modes. The oscillation frequency of the reconstructed energy in (*d–f*) is twice that of the VS frequency.

present throughout, they are energetically more prominent in the far-wake region. It is interesting to note that beyond $x/D \approx 65$, the defect velocity decay rate changes from x^{-1} to $x^{-2/3}$ in the wake (Chongsiripinyo & Sarkar 2020). For comparison, the most dominant component at the zeroth frequency, i.e. $m = 2$, is also shown in figure 9(*b*), which exhibits a similar trend of increasing prominence in the downstream direction.

Having diagnosed the streaky structure ($m = 2$, $St \to 0$) and the VS structure ($m = 1$, $St = 0.135$) using SPOD, we shift focus to their imprint on the flow in physical space by reconstructing the flow field using their leading five SPOD modes. The $m = 2$ wavenumber is selected because it is energetically dominant at $St \to 0$. The reconstruction is performed using the convolution strategy described in § 2. Figures 10(*a–c*) show the instantaneous energy in the three fluctuation components u'_x, u'_r and u'_θ at $x/D = 10$, 40 and 80, after reconstruction with the streaky-structure SPOD modes. The instantaneous energy is depicted within the time interval $t \in [0, 110]$, which corresponds to the first five blocks used for SPOD, and is representative of the entire reconstructed flow fields. The energy of u'_x is significantly higher than that of u'_r and u'_θ. The dominance of the streamwise component over its radial and azimuthal counterparts is one salient feature of streaks. The finding of u'_x dominance is in agreement with results of Boronin, Healey & Sazhin (2013, see figure 11) and Pickering *et al.* (2020, see figure 10) in the context of round jets, indicating similarity in streak formation between jets and wakes. The lift-up mechanism, in which the streamwise vortices lift up and push down the low-speed and high-speed fluid, respectively, is responsible for elongated streaks accompanied by an amplification of u'_x. The analogues of figures 10(*a–c*) are shown for the VS mode in figures 10(*d–f*). Here, u'_x and u'_r components have comparable energy, showing a fundamental difference between the VS mode and the streaky-structures mode as to how each mode contributes to velocity fluctuations in the wake. Furthermore, the instantaneous energy of the flow field

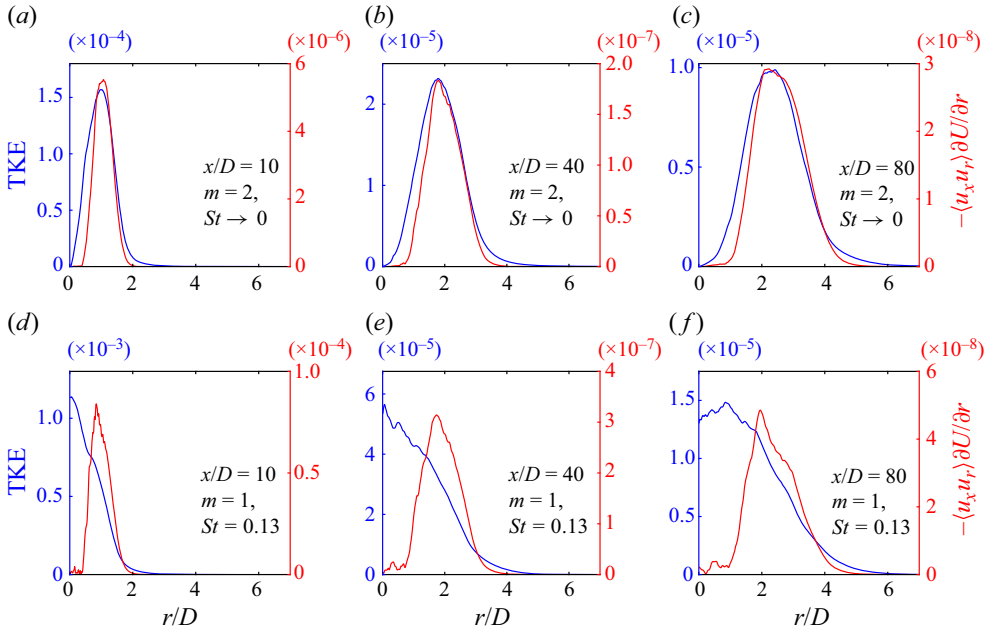

Figure 11. TKE and production due to shear at different downstream locations for the flow fields reconstructed from (*a–c*) the streaky-structures mode, and (*d–f*) VS mode. Plot (*a,d*) correspond to $x/D = 10$, (*b,e*) to $x/D = 40$, and (*c,f*) to $x/D = 80$. Flow reconstruction uses the leading five SPOD modes.

reconstructed from the VS mode has a much smaller time scale in comparison to that of the large-scale streaks.

Figure 11 shows the TKE ($K = \langle u_i' u_i' \rangle/2$) and its shear production ($P_{xr} = -\langle u_x' u_r' \rangle \partial U/\partial r$) corresponding to the large-scale streaks and VS structures at $x/D = 10$, 40 and 80. As in figure 10, TKE and P_{xr} are computed from the leading five SPOD modes. Figures 11(*a–c*) show that the TKE and the production peak at similar radial locations for $m = 2$, $St \to 0$. This is not the case for $m = 1$, $St = 0.135$ (figures 11*d–f*), where the peak TKE occurs close to the centreline, while the production peaks away from the centreline. This difference in the locations of peak K and P_{xr} indicates that turbulent transport plays an important role in distributing the TKE in the VS mode, similar to its importance in the full TKE budget of an axisymmetric wake (Uberoi & Freymuth 1970). The difference in radial locations of peak K and P_{xr}, as demonstrated in figure 11, is another crucial distinction between the large-scale streaky mode and the VS mode. The presence of streaks is associated with high TKE around the region of high production/mean shear, indicating their important role in the energy transfer from mean to fluctuation velocity in the turbulent wake, similar to other shear flows (Gualtieri *et al.* 2002; Brandt 2007; Jiménez-González & Brancher 2017). As a result, the TKE achieves its global maximum around the same location as that of P_{xr} for streaks.

4.2. *Lift-up mechanism through the lens of SPOD analysis*

Subsection 4.1 demonstrated that the structures associated with $St \to 0$ exhibit the characteristics of streaks, and their significance increases from near to far wake, with the azimuthal wavenumber $m = 2$ being the most significant, energetically, to the streaks.

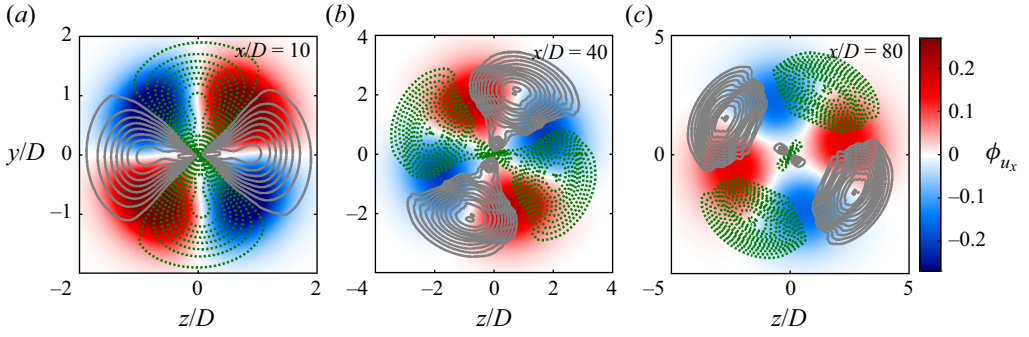

Figure 12. Leading SPOD mode of $m = 2$ and $St \to 0$, for (*a*) $x/D = 10$, (*b*) $x/D = 40$, and (*c*) $x/D = 80$. The false colours represent the real part of the streamwise velocity component $\mathrm{Re}[\phi^{(1)}_{u_x}(St \to 0)]$, and the grey lines and green dotted lines correspond to positive and negative streamwise vorticity $\mathrm{Re}[\phi^{(1)}_{\omega_x}(St \to 0)]$, respectively.

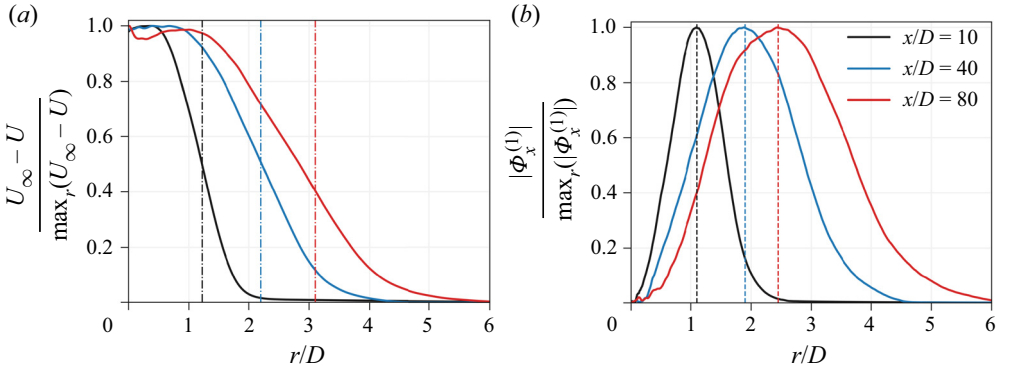

Figure 13. (*a*) Normalized mean defect velocity ($U_d = U_\infty - U$) profiles. (*b*) Normalized leading SPOD mode of the streamwise velocity (u_x) at $m = 2$ and $St \to 0$. Dashed lines in (*a*) and dot-dashed lines in (*b*) correspond to the radial location of the maximum of SPOD mode and the maximum of mean shear ($\partial U/\partial r$), respectively.

Figure 12 shows the leading SPOD mode of the streamwise velocity fluctuation (u'_x) corresponding to $m = 2$ and $St \to 0$ at three streamwise locations, $x/D = 10$, 40 and 80. Overlaid on the u'_x contour is the streamwise vorticity (ω'_x) of the corresponding mode. Both u'_x and ω'_x are characterized by four lobes of alternate sign, the sizes of which increase monotonically with x/D. Importantly, the set of ω'_x lobes is shifted with respect to the u'_x lobes by a clockwise rotation of approximately 45°. As a result of the shift, the maximum of u'_x in the mode appears at the location where the vortices bring in high-speed fluid from the outer to the inner wake, and vice versa. This observation further confirms the presence of the lift-up mechanism in the wake.

Figure 13(*a*) shows the normalized radial profiles of mean defect velocity (U_d) at $x/D = 10, 40, 80$. Figure 13(*b*) shows the radial profile of the normalized leading SPOD mode's streamwise component for $m = 2$, $St \to 0$, at the same streamwise locations as in figure 13(*a*). As the wake develops in the x direction, the location of mode maximum shifts away from the centreline. A visual comparison shows that the location of amplitude maximum (dashed lines in figure 13*b*) of the dominating streak-containing mode lies in close proximity to the location of the maximum mean shear (dot-dashed lines in

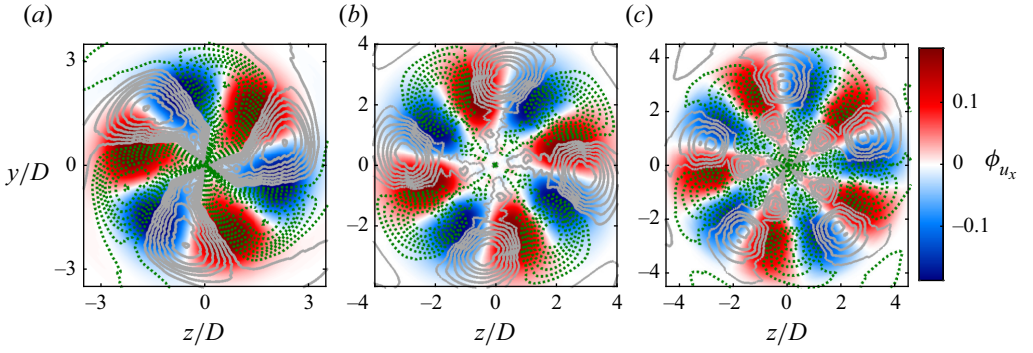

Figure 14. Leading SPOD mode at $x/D = 40$ and $St \to 0$ for higher azimuthal wavenumbers, for (*a*) $m = 3$, (*b*) $m = 4$, and (*c*) $m = 5$. The false colours represent $\mathrm{Re}[\phi^{(1)}_{u_x}(St \to 0)]$, and the grey lines and green dotted lines correspond to the positive and negative values of streamwise vorticity $\mathrm{Re}[\phi^{(1)}_{\omega_x}(St \to 0)]$.

figure 13*a*). The large radial gradient of the streamwise velocity induces a positive mean vorticity, lifting up the low-speed fluid from the inner wake to form streaks. Hence an extremum in u'_x appears in the SPOD mode. The seminal work of Ellingsen & Palm (1975) demonstrates that for linearized disturbances in an inviscid flow, $\partial u_x/\partial t \propto -u_r\, \partial U(r)/\partial r$, and the lift-up mechanism is most active in the region closest to the largest mean shear. So is the case in the present turbulent wake.

The lift-up mechanism is also active at higher azimuthal wavenumbers, as demonstrated by figure 14, which shows the leading SPOD modes at $x/D = 40$ and frequency $St \to 0$ for the higher modes, $m = 3$, 4 and 5. Similar to figure 12, positive and negative streamwise velocity contours are encompassed by counter-rotating vortices that move the fluid from the fast- to slow-speed regions, and vice versa. The radial spread of the streamwise velocity lobes increases with m, and the number of lobes scales as $2m$. Also, the vortices are shifted by 30°, 22.5° and 18°, for $m = 3$, 4 and 5, respectively. In other words, the set of streamwise velocity lobes for wavenumber m is shifted by an angle $\pi/2m$ radians with respect to the streamwise vortices. As in the case of $m = 2$, the peak of the leading SPOD modes for $m = 3, 4, 5$ lies in the vicinity of the maximum mean shear. Even for higher m, the lift-up effect occurs nears the region of the largest mean shear. This further confirms that the lift-up mechanism is active for higher azimuthal wavenumbers.

5. Analysis of triadic interactions in the wake

Previous sections show that the streaks are present predominantly in the $m = 2$ azimuthal mode. To shed light on the possible dynamics behind the formation of streaks in a turbulent wake, we focus on the nonlinear interactions between the VS-containing $m = 1$ mode and the streak-containing $m = 2$ mode.

5.1. *Bispectral mode decomposition at select locations*

Figure 15 shows the SPOD spectra for the azimuthal wavenumbers $m = 1$ and $m = 2$ at $x/D = 10$. Both SPOD spectra exhibit a large difference between the first and second eigenvalues for $St \lesssim 0.5$, thus demonstrating a low-rank behaviour. The leading eigenvalue of the $m = 1$ azimuthal mode peaks at the VS frequency $St = 0.135$. On the other hand, the leading eigenvalue of the $m = 2$ azimuthal mode exhibits a global peak

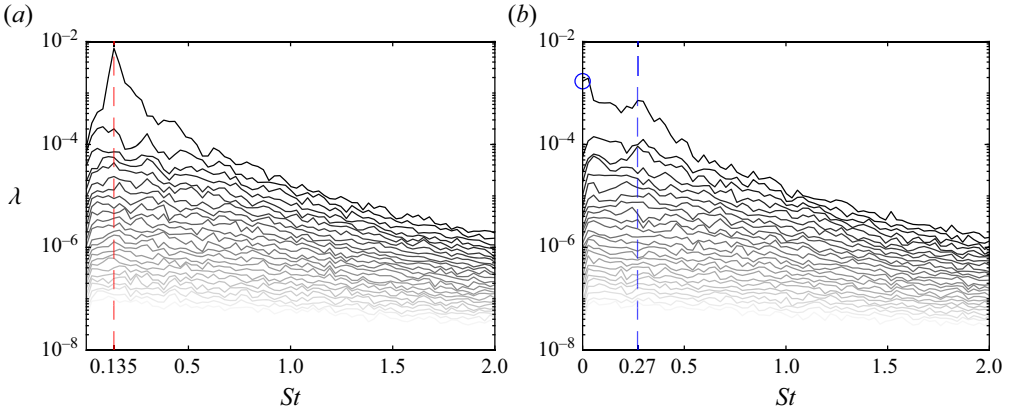

Figure 15. SPOD spectra at $x/D = 10$, for (*a*) $m = 1$, and (*b*) $m = 2$. Dashed red and blue lines in (*a*) and (*b*) correspond to $St = 0.135$ and $St = 0.27$, respectively.

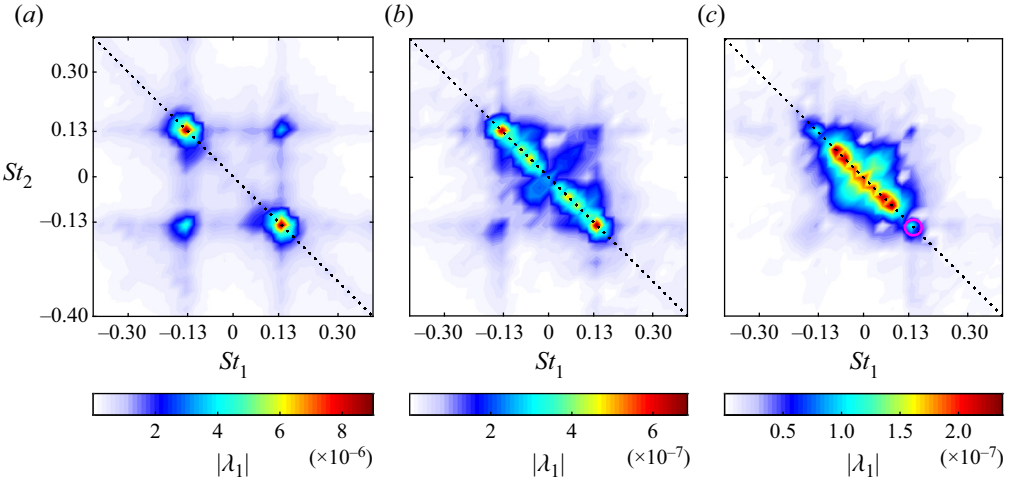

Figure 16. Cross-BMD spectra for the azimuthal triad $[m_1, m_2, m_3 = m_1 + m_2] = [1, 1, 2]$, for (*a*) $x/D = 10$, (*b*) $x/D = 40$, and (*c*) $x/D = 80$. The black dotted line denotes $St_1 + St_2 = St_3 = 0$.

at $St \to 0$, and an additional local peak at $St = 0.27$ (blue dashed line in figure 15). Furthermore, Nidhan *et al.* (2020, see their figure 20) find that the VS mode gains prominence at $x/D \approx 1$, while the peak corresponding to $m = 2$, $St \to 0$ appears further downstream, at $x/D \approx 5$. Collectively, these observations point towards different sets of triadic interactions involving the VS mode. For example, $m = 1$, $St = 0.135$ can interact with $m = 1$, $St = -0.135$ to give rise to $m = 2$, $St \to 0$ that appears further downstream. Similarly, the self-interaction of $m = 1$, $St = 0.135$ can generate $m = 2$, $St = 0.27$ (local peak denoted by dashed line in figure 15*b*). In what follows, we demonstrate quantitatively the presence of these triadic interactions at select x/D locations using BMD (Schmidt 2020).

Figure 16 shows the cross-mode bispectra for the azimuthal wavenumber triad $[m_1, m_2, m_3] = [1, 1, 2]$, at three axial locations, $x/D = 10$, 40 and 80. These spectra

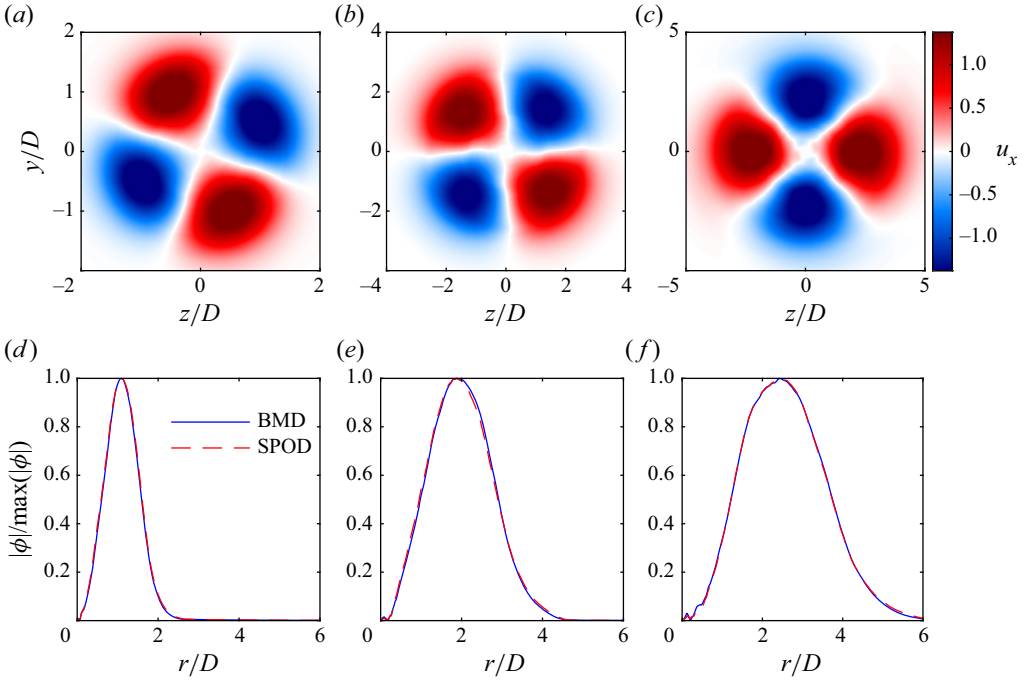

Figure 17. Cross-BMD modes for the triad [1, 1, 2] in azimuth and (0.135, −0.135, 0) in frequency, at three streamwise locations: (*a*) $x/D = 10$, (*b*) $x/D = 40$, and (*c*) $x/D = 80$. The false colours represent the real part of the streamwise velocity component. The absolute value of the BMD mode and the corresponding leading SPOD mode are compared in (*d*)–(*f*).

provide a measure of the interaction among the three azimuthal components. The abscissa (St_1) and ordinate (St_2) of the BMD spectra correspond to the frequencies of the m_1 mode and m_2 mode, respectively. Here, $m_1 = 1$, $m_2 = 1$ and $m_3 = 2$. The high-intensity regions in the spectra represent the energetically dominant triads. In figure 16, the mode bispectra are symmetric about the diagonal $St_1 = St_2$. At $x/D = 10$ (figure 16*a*), the most dominant triad is (0.135, −0.135, 0), and other significant triads are (0.135, 0.135, 0.27) and (−0.135, −0.135, −0.27). This observation confirms the presence of triadic interactions hypothesized in the context of figure 15, and emphasizes that the strongest triadic nonlinear interaction is between the VS mode ($m = 1$, $St = 0.135$), its conjugate ($m = 1$, $St = -0.135$), and streaks ($m = 2$, $St \to 0$). A similar observation is made from the mode bispectra at $x/D = 40$. At $x/D = 80$, the most dominant triad occurs at (0.09, −0.09, 0) and along the $St_1 = -St_2$ line, but a local maximum (marked by a circle in magenta) is still present at (0.135, −0.135, 0), which indicates that the triadic interaction between the VS mode and its complex conjugate leading to streaks is still active, albeit subdominant. From figure 16, we infer that the triadic interaction between [1, 1, 2] at (0.135, −0.135, 0) is prominent in the near wake, and its intensity decreases progressively downstream. It is important to note that when all interactions with $[m_1, St_1, m_2, St_2]$ such that $St_1 + St_2 = 0$ were quantified (not shown here for brevity), that between $m_1 = m_2 = 1$ and $St_{1,2} = \pm 0.135$ was found to be the strongest.

Next, we visualize the structures associated with the triadic interaction of the VS mode, its conjugate, and streaks in figure 17. The real part of the streamwise velocity component of the corresponding cross-bispectral modes is shown at $x/D = 10$, 40 and 80. Similar to figure 12, the radial extent of these modes increases downstream, and they exhibit four

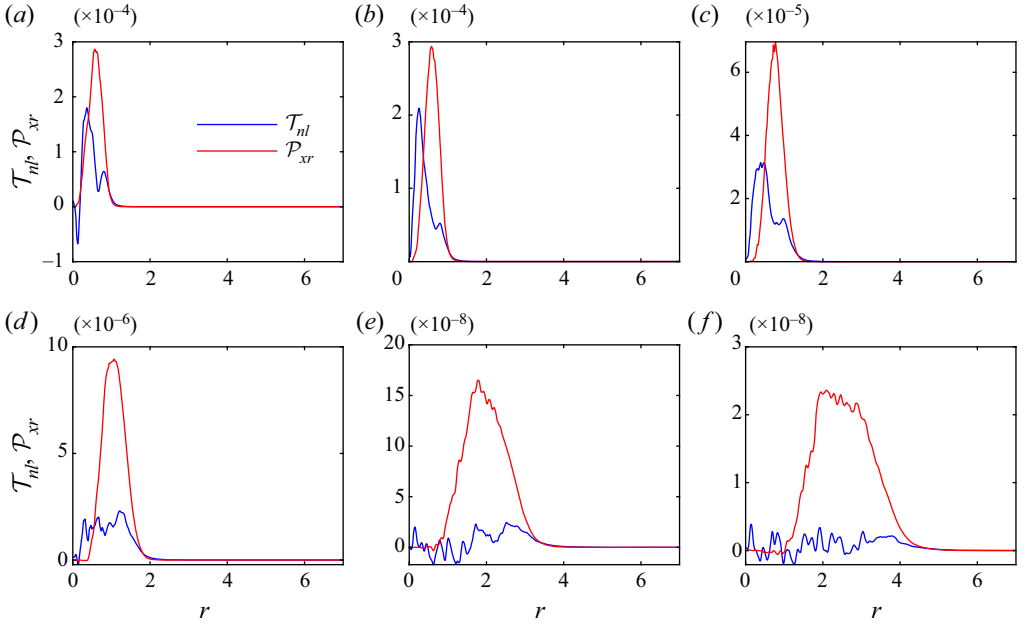

Figure 18. Nonlinear transfer ($\mathcal{T}_{nl}$) from the VS mode and the shear production ($\mathcal{P}_{xr}$) at different streamwise locations for the $m = 2$, $St \to 0$ mode, for (*a*) $x/D = 2$, (*b*) $x/D = 3$, (*c*) $x/D = 5$, (*d*) $x/D = 10$, (*e*) $x/D = 40$, and (*f*) $x/D = 80$.

lobes of alternate signs. For a more quantitative comparison, figures 17(*d–f*) show the magnitudes of the modes normalized by their maximum value. The corresponding curves are coincident, indicating that the spatial structures generated by the triadic interactions are also the most energetic coherent structures. This further confirms that the $m = 2$, $St \to 0$ mode is indeed generated through the interaction of $St = \pm 0.135$ at the $m = 1$ azimuthal mode.

5.2. *Comparison between nonlinear interactions and the linear lift-up mechanism*

Finally, the relative role of nonlinear interaction and the linear lift-up mechanism in streak energetics is examined. In figure 18, $\mathcal{P}_{xr}$ denotes shear production in the $m = 2$, $St \to 0$ mode, and $\mathcal{T}_{nl}$ denotes nonlinear energy transfer from $m = 1$, $St = \pm 0.135$ modes to the $m = 2$, $St \to 0$ mode. These two terms are defined in Appendix C. Figure 18 reveals that both terms are comparable in magnitude and of the same sign for $x/D \leq 5$, whereas $\mathcal{P}_{xr}$ dominates beyond $x/D = 10$. Thus, near the wake generator, both (i) the nonlinear interaction of the VS mode with its conjugate, and (ii) the linear production due to the lift-up process, are of similar importance to streak energetics. Beyond the near wake, the linear mechanism is responsible for maintaining the streaks.

6. Discussion and conclusions

Streaks, which are coherent elongated regions of streamwise velocity, have been found in a variety of turbulent shear flows. However, they have not received attention in turbulent wakes motivating the present examination of an LES dataset of flow past a disk at $Re = 50\,000$ (Chongsiripinyo & Sarkar 2020). Visualizations and SPOD are employed, and they

reveal the presence of streaks from the near wake to the outflow at $x/D \approx 120$. Until now, most of the wake literature has understandably focused on the VS structure ($m = 1$, $St = 0.135$ for the circular disk), since it is the energetically dominant coherent structure in the near and intermediate wake. Upon removing the contribution of the $m = 1$ azimuthal wavenumber *a priori* in visualizations, the streaks become evident, even in the near and intermediate wake. Moreover, in the far wake ($x/D \geq 70$), it is the streaks that become the energetically dominant coherent structure. To the best of our knowledge, this is the first study that reports the existence of streaks in turbulent wakes. These results re-emphasize that mean shear, not a wall boundary condition, is a necessary condition for the existence of streaks (Jiménez & Pinelli 1999; Mizuno & Jiménez 2013; Nogueira *et al.* 2019).

Streaks differ from VS structures in three key ways: (i) they exhibit a much larger wavelength and time scale; (ii) VS structures are tilted with respect to the downstream direction, whereas streaks are almost parallel; (iii) the streamwise velocity (u'_x) significantly exceeds the other two velocity components (u'_r, u'_θ) in magnitude for streaks, whereas u'_x and u'_r are comparable for VS structures. The streaky structures are associated with frequency $St \to 0$ and hence, by Taylor's hypothesis (validated here for the wake) to wavenumber $k_x \to 0$. While streaky structures are observed for all non-zero azimuthal wavenumbers, $m = 2$ dominates in the near-to-far wake. In particular, SPOD analysis reveals that $m = 2$ contains about 55 % (near wake) to 40 % (far wake) of the total energy of streaks. This is in contrast to turbulent jets, where Pickering *et al.* (2020) show that the dominant azimuthal wavenumber (m_{dom}) at $St \to 0$ varies as $m_{dom} \sim 1/x$, implying that higher m and not $m = 2$ would be dominant near the jet nozzle. It is worth noting that only two studies (Johansson & George 2006; Nidhan *et al.* 2020) have reported the importance of $m = 2$, $St \to 0$ in turbulent wakes; however, they do not link this mode to streaks.

We find that the lift-up mechanism is active in turbulent wakes, similar to wall-bounded shear flows (Abreu *et al.* 2020) and turbulent jets (Nogueira *et al.* 2019; Lasagna *et al.* 2021). Conditional averaging and SPOD analysis demonstrate clearly that streamwise vortices lift up low-speed fluid from the wake's core and push down high-speed fluid from the outer wake. It is also observed that the lift-up mechanism is spatially most active in the vicinity of the largest mean shear and TKE production, indicating that energy is transferred directly from the mean flow to the velocity fluctuations in the streaks. The lift-up process triggered by the streamwise vortices shows a similar energy transfer mechanism in turbulent pipe flow (Hellström, Marusic & Smits 2016) and homogeneous shear flow (Gualtieri *et al.* 2002; Brandt 2014).

The lift-up mechanism results in the formation of both low-speed and high-speed streaks. These low- and high-speed streaks exhibit large negative values of Reynolds shear stress. Conditional averaging of streamwise vorticity fluctuations, performed based on peak negative Reynolds shear stress, shows that the ejection of low-speed fluid from the wake's core is more dominant than the sweep of the high-speed fluid from the outer wake. The boundary layers also exhibit a similar phenomenon, where ejections are a greater contributor to Reynolds shear stress than sweeps (Kline *et al.* 1967; Lu & Willmarth 1973).

Beyond identification of streaks, we also explore the role of nonlinear interactions in the context of wake streaks. Specifically, BMD is used to investigate the nonlinear interactions between the $m = 1$, $St = \pm 0.135$ VS mode and the $m = 2$, $St \to 0$ streak mode. The $m = 1$, $St = \pm 0.135$ vortices are found to interact and generate the $m = 2$, $St \to 0$ vortices. These streamwise vortices of the $m = 2$, $St \to 0$ mode then lift up low-speed fluid from the inner wake and push down the high-speed fluid from the outer wake (figure 12), resulting in the formation of streaks. This suggests that the wake has a phenomenon analogous to the

'regeneration cycle' (Hamilton *et al.* 1995; Farrell & Ioannou 2012) of wall-bounded flows, which involves the generation of streamwise vortices through nonlinear interactions, and the formation of streaks through linear advection by these streamwise vortices. Recently, Bae *et al.* (2021) have shown that the nonlinear interactions between spanwise rolls and oblique streaks regenerate streamwise vortices, which then amplify streaks through the lift-up mechanism in wall-bounded flows.

This work demonstrates that streaks and the associated lift-up mechanism are operative in the turbulent disk wake. The results also open directions for future research. Previous work by Ortiz-Tarin, Nidhan & Sarkar (2021, 2023) on the wake of a slender 6 : 1 prolate spheroid found that the wake differs significantly from its bluff body counterpart. Therefore, one possible direction is to investigate how the shape of the wake generator affects the streaky structures and the lift-up mechanism. Moreover, the influence of the angle of attack and surface properties (roughness, porosity) on the development of these structures could be explored. Also, it is worth investigating how density stratification (Nidhan, Schmidt & Sarkar 2022; Gola *et al.* 2023), often found in the natural environment, affects the lift-up mechanism and formation of streaks in turbulent disk wakes. Finally, a direct comparison of the characteristics of streaks in wakes, such as length scales, intermittency and life cycle, with those in other turbulent flows, such as channel flows and jets, can inform about potentially universal behaviour of streaks in turbulent flows. In the same vein, it will be also interesting to build reduced-order models to isolate and understand the spatiotemporal features of interaction between the VS mode and streaks, as was done with a problem with Kelvin–Helmholtz-like instabilities and streaks (Nogueira & Cavalieri 2021; Cavalieri, Rempel & Nogueira 2022).

Acknowledgements. We thank Dr K. Chongsiripinyo for the disk wake database.

Funding. We acknowledge the support of Office of Naval Research (ONR) grant N00014-20-1-2253.

Declaration of interests. The authors report no conflict of interest.

Author ORCIDs.
Akhil Nekkanti https://orcid.org/0000-0002-2173-8704;
Sheel Nidhan https://orcid.org/0000-0003-0433-6129;
Oliver T. Schmidt https://orcid.org/0000-0002-7097-0235;
Sutanu Sarkar https://orcid.org/0000-0002-9006-3173.

Author contributions. A.N. and S.N. have contributed equally to this paper and are co-first authors.

Appendix A. Effect of parameter n_{fft} on the frequency of the large-scale streaks

Here, the parameter n_{fft} is varied to identify the true frequency of the streaks in the wake. Due to the constraint of the time series length, the power spectral density (PSD) and SPOD spectra corresponding to the streaks peak in the first frequency bin and are hence interpreted as $St \to 0$. For better resolution, one can increase n_{fft}. However, this results in an increase in variance. Hence we employ the multitaper-Welch based PSD (Thomson 1982) and SPOD (Schmidt 2022) as it outperforms the standard Welch estimator in terms of variance and resolution (Bronez 1992). Recently, Nekkanti & Schmidt (2023) have shown that the parameters n_{fft} and n_{ovlp} can significantly affect the spectrum and reconstruction of data. Figure 19 shows the PSD and SPOD performed using $n_{fft} = 1024$, 2048, 4096 and 7132 with $N_{win} = 10$ Slepian tapers as windows. The PSD is computed at $x/D = 40$, $r/D = 2$, and SPOD spectra at $x/D = 40$. As the goal is to identify the true frequency, we plot the spectra for $St > 0$. For figures 19(a,b,e,f), as n_{fft} is not large enough,

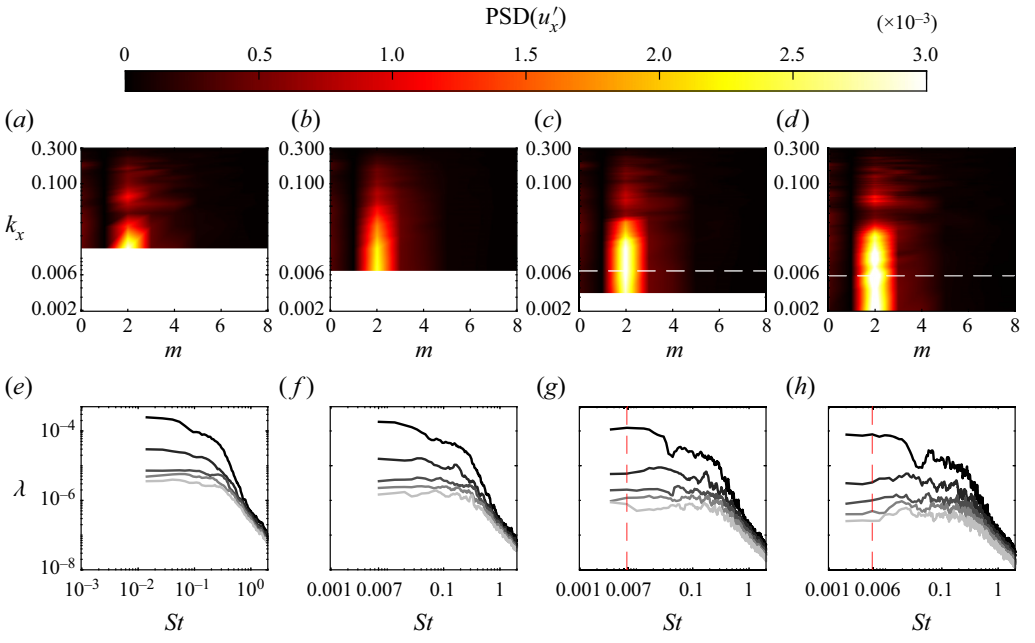

Figure 19. Effect of n_{fft} and tapers on (*a–d*) the PSD at $r/D = 2$, $x/D = 40$, and (*e–h*) SPOD at $x/D = 40$, for: (*a*,*e*) $n_{fft} = 1024$, $N_{win} = 10$; (*b*,*f*) $n_{fft} = 2048$, $N_{win} = 10$; (*c*,*g*) $n_{fft} = 4096$, $N_{win} = 10$; (*d*,*h*) $n_{fft} = 7132$, $N_{win} = 10$. The white and red lines correspond to the peak in PSD and SPOD spectra. The PSD and SPOD spectra are plotted for $St > 0$.

the peak in the PSD and SPOD is at $St \to 0$. On increasing the n_{fft}, two-dimensional PSD and SPOD spectra can resolve the lower frequencies, and their peak approaches $St \approx 0.006$ at the highest possible n_{fft} (figures 19*d*,*h*). Using this approach, the frequency associated with the large-scale streaky structures can be identified, which is $St \approx 0.006$. Note that the availability of more snapshots will result in a better convergence of the peak frequency associated with streaks.

Appendix B. Conditional averaging: sensitivity of parameter *c*

Figures 20 and 21 show the effect of varying c in (3.1) and (3.2) on the obtained $\langle \omega_x^{c1} \rangle$ and $\langle \omega_x^{c2} \rangle$ fields, respectively, at a representative location of $x/D = 40$. In both figures, changing c between 0 and 1 has little qualitative effect on the distribution of negative and positive vortices around the conditioning point. It is interesting to note, however, that the $\langle \omega_x^{c2} \rangle$ field is more robust to changes in c than the $\langle \omega_x^{c1} \rangle$ field. Increasing the value of c leads to the capture of more intense events, but it also reduces the number of realizations available for averaging. Hence, based on figure 7, $c = 0.5$ is selected as a compromise between capturing intense events and having sufficient realizations for temporal averaging.

Appendix C. Scale-specific production and nonlinear transfer terms in the disk wake for $m = 2$, $St \to 0$ mode

Fourier modes and Welch estimation are employed to compute the scale-specific production and nonlinear transfer terms. The mathematical forms of these two terms are as follows.

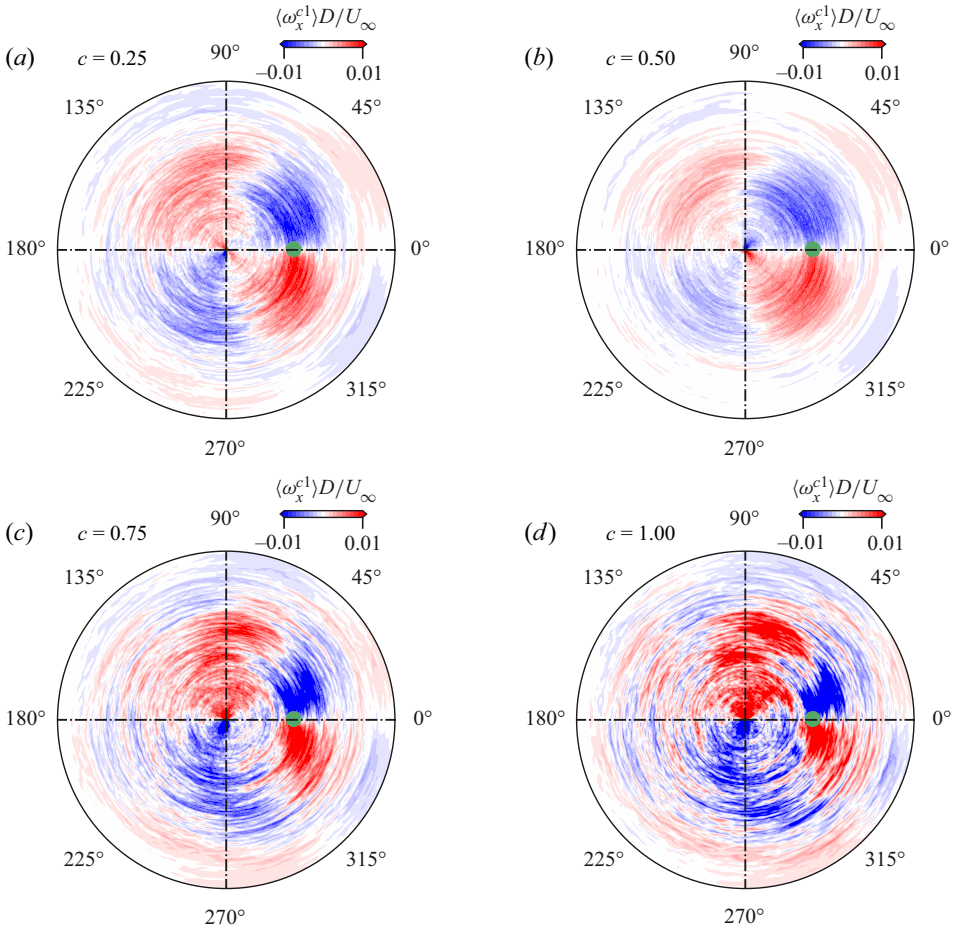

Figure 20. Effect of changing c on the conditionally averaged streamwise vorticity $\langle\omega_x^{c1}\rangle$ obtained from u_x' based conditioning at $x/D = 40$.

The scale-specific production term is

$$\mathcal{P}(m, St) = -\mathrm{Re}\left[\hat{u}_j^*(m, St)\,\hat{u}_i(m, St)\,\frac{\partial U_j}{\partial x_i}\right], \tag{C1}$$

where, Re[·] denotes the real part. We are interested specifically in the production term by lateral mean shear operating on the $m = 2$, $St \to 0$ mode:

$$\mathcal{P}_{xr}(m = 2, St \to 0) = -\mathrm{Re}\left[\hat{u}_x^*\hat{u}_r\,\frac{\partial U}{\partial r}\right]_{(m=2,\ St\to 0)}. \tag{C2}$$

The scale-specific nonlinear transfer is

$$\mathcal{T}_{nl}(m, St) = -\mathrm{Re}\left[\hat{u}_j^*(m, St)\,\widehat{u_i\,\frac{\partial u_j}{\partial x_i}}(m, St)\right]. \tag{C3}$$

This term represents the total nonlinear transfer term that generates the frequency St and wavenumber m. For identifying the triadic energy transfer, i.e. $m_1 + m_2 = m_3$ and

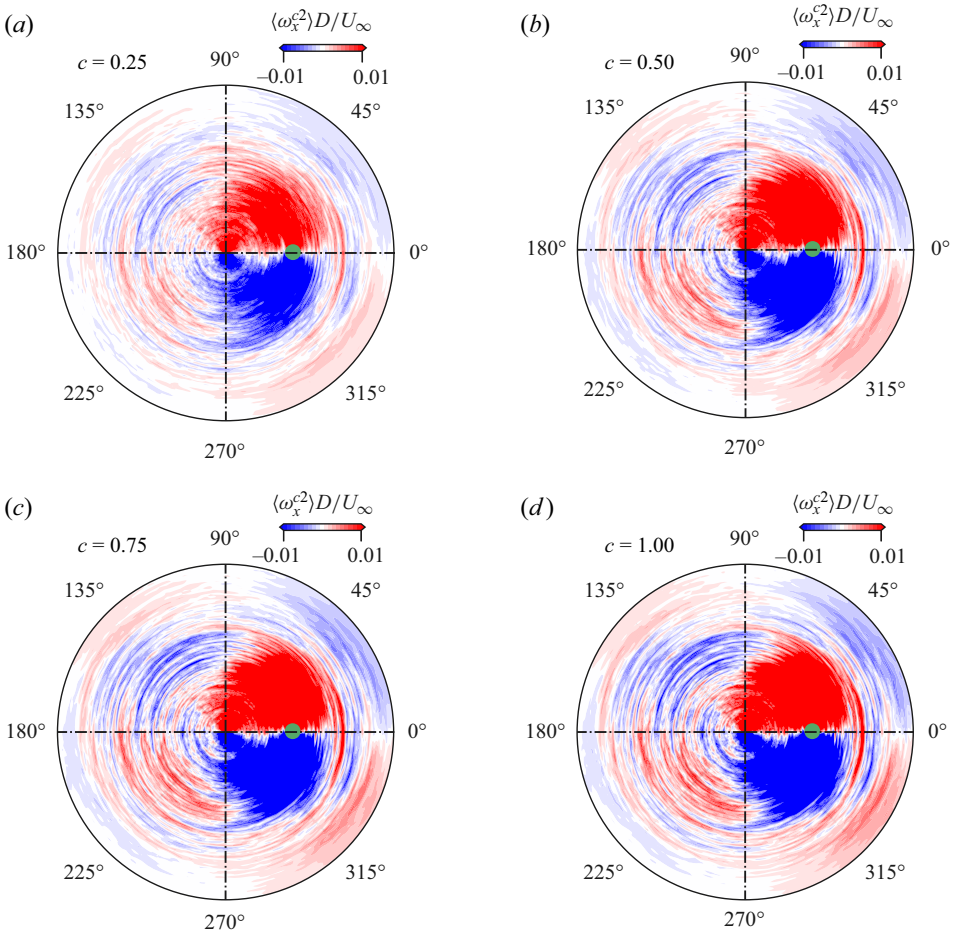

Figure 21. Effect of changing c on the conditionally averaged streamwise vorticity $\langle\omega_x^{c2}\rangle$ obtained from $u_x'u_r'$ based conditioning at $x/D = 40$.

$St_1 + St_2 = St_3$, following Cho, Hwang & Choi (2018), we write this term in discretized convolution as

$$\mathcal{T}_{nl}(m_3, St_3) = -\mathrm{Re}\left[\hat{u}_j^*(m_3, St_3) \sum_{\substack{St_1+St_2=St_3 \\ m_1+m_2=m_3}} \hat{u}_i(m_1, St_1)\, \frac{\partial \hat{u}_j}{\partial x_i}(m_2, St_2)\right]. \tag{C4}$$

For a single triad $[m_1, m_2, m_3]$, $[St_1, St_2, St_3]$, this is expanded as

$$\mathcal{T}_{nl}[(m_1, m_2, m_3), (St_1, St_2, St_3)] = -\mathrm{Re}\left[\hat{u}_j^*(m_3, St_3)\, \hat{u}_i(m_1, St_1)\, \frac{\partial \hat{u}_j}{\partial x_i}(m_2, St_2)\right]. \tag{C5}$$

The nonlinear term of our interest is the one responsible for transfer of energy from the VS mode to the $m = 2$, $St \to 0$ mode:

$$\mathcal{T}_{nl}[(1, 1, 2), (0.135, -0.135, 0)] = -\mathrm{Re}\left[\hat{u}_j^*(2, 0)\, \hat{u}_i(1, 0.135)\, \frac{\partial \hat{u}_j}{\partial x_i}(1, -0.135)\right]. \tag{C6}$$

References

Abreu, L.I., Cavalieri, A.V.G., Schlatter, P., Vinuesa, R. & Henningson, D.S. 2020 Spectral proper orthogonal decomposition and resolvent analysis of near-wall coherent structures in turbulent pipe flows. *J. Fluid Mech.* **900**, A11.

Antonia, R.A. & Mi, J. 1998 Approach towards self-preservation of turbulent cylinder and screen wakes. *Exp. Therm. Fluid Sci.* **17** (4), 277–284.

Bae, H.J., Lozano-Duran, A. & McKeon, B.J. 2021 Nonlinear mechanism of the self-sustaining process in the buffer and logarithmic layer of wall-bounded flows. *J. Fluid Mech.* **914**, A3.

Balaras, E. 2004 Modeling complex boundaries using an external force field on fixed Cartesian grids in large-eddy simulations. *Comput. Fluids* **33** (3), 375–404.

Berger, E., Scholz, D. & Schumm, M. 1990 Coherent vortex structures in the wake of a sphere and a circular disk at rest and under forced vibrations. *J. Fluids Struct.* **4** (3), 231–257.

Bernal, L.P. & Roshko, A. 1986 Streamwise vortex structure in plane mixing layers. *J. Fluid Mech.* **170**, 499–525.

Boronin, S.A., Healey, J.J. & Sazhin, S.S. 2013 Non-modal stability of round viscous jets. *J. Fluid Mech.* **716**, 96–119.

Brandt, L. 2007 Numerical studies of the instability and breakdown of a boundary-layer low-speed streak. *Eur. J. Mech. (*B*/Fluids)* **26** (1), 64–82.

Brandt, L. 2014 The lift-up effect: the linear mechanism behind transition and turbulence in shear flows. *Eur. J. Mech. (*B*/Fluids)* **47**, 80–96.

Bronez, T.P. 1992 On the performance advantage of multitaper spectral analysis. *IEEE Trans. Signal Process.* **40** (12), 2941–2946.

Brown, G.L. & Roshko, A. 1974 On density effects and large structure in turbulent mixing layers. *J. Fluid Mech.* **64** (4), 775–816.

Cannon, S., Champagne, F. & Glezer, A. 1993 Observations of large-scale structures in wakes behind axisymmetric bodies. *Exp. Fluids* **14** (6), 447–450.

Cavalieri, A.V.G., Rempel, E.L. & Nogueira, P.A.S. 2022 Transition to chaos in a reduced-order model of a shear layer. *J. Fluid Mech.* **932**, A43.

Cho, M., Hwang, Y. & Choi, H. 2018 Scale interactions and spectral energy transfer in turbulent channel flow. *J. Fluid Mech.* **854**, 474–504.

Chongsiripinyo, K. & Sarkar, S. 2020 Decay of turbulent wakes behind a disk in homogeneous and stratified fluids. *J. Fluid Mech.* **885**, A31.

Corino, E.R. & Brodkey, R.S. 1969 A visual investigation of the wall region in turbulent flow. *J. Fluid Mech.* **37** (1), 1–30.

Dairay, T., Obligado, M. & Vassilicos, J.C. 2015 Non-equilibrium scaling laws in axisymmetric turbulent wakes. *J. Fluid Mech.* **781**, 166–195.

Delville, J. 1994 Characterization of the organization in shear layers via the proper orthogonal decomposition. *Appl. Sci. Res.* **53** (3), 263–281.

Ellingsen, T. & Palm, E. 1975 Stability of linear flow. *Phys. Fluids* **18** (4), 487.

Farrell, B.F. & Ioannou, P.J. 2012 Dynamics of streamwise rolls and streaks in turbulent wall-bounded shear flow. *J. Fluid Mech.* **708**, 149–196.

Fuchs, H.V., Mercker, E. & Michel, U. 1979*a* Large-scale coherent structures in the wake of axisymmetric bodies. *J. Fluid Mech.* **93** (1), 185–207.

Fuchs, H.V., Mercker, E. & Michel, U. 1979*b* Large-scale coherent structures in the wake of axisymmetric bodies. *J. Fluid Mech.* **93** (1), 185–207.

Germano, M., Piomelli, U., Moin, P. & Cabot, W.H. 1991 A dynamic subgrid-scale eddy viscosity model. *Phys. Fluids* **3** (7), 1760–1765.

Glauser, M.N. & George, W.K. 1992 Application of multipoint measurements for flow characterization. *Exp. Therm. Fluid Sci.* **5** (5), 617–632.

Glauser, M.N., Leib, S.J. & George, W.K. 1987 Coherent structures in the axisymmetric turbulent jet mixing layer. In *Turbulent Shear Flows 5*, pp. 134–145. Springer.

Gola, D., Nidhan, S., Ortiz-Tarin, J.L. & Sarkar, S. 2023 Disk wakes in nonlinear stratification. *J. Fluid Mech.* **956**, A5.

Goparaju, H. & Gaitonde, D.V. 2022 Role of entropic instabilities in laminar–turbulent transition on a blunted flat plate. *Phys. Rev. Fluids* **7** (10), 103901.

Gualtieri, P., Casciola, C.M., Benzi, R., Amati, G. & Piva, R. 2002 Scaling laws and intermittency in homogeneous shear flow. *Phys. Fluids* **14** (2), 583–596.

Hamilton, J.M., Kim, J. & Waleffe, F. 1995 Regeneration mechanisms of near-wall turbulence structures. *J. Fluid Mech.* **287**, 317–348.

HELLSTRÖM, L.H.O., MARUSIC, I. & SMITS, A.J. 2016 Self-similarity of the large-scale motions in turbulent pipe flow. *J. Fluid Mech.* **792**, R1.

HUTCHINS, N. & MARUSIC, I. 2007 Evidence of very long meandering features in the logarithmic region of turbulent boundary layers. *J. Fluid Mech.* **579**, 1–28.

JIMÉNEZ, J. 2018 Coherent structures in wall-bounded turbulence. *J. Fluid Mech.* **842**, P1.

JIMÉNEZ, J. & PINELLI, A. 1999 The autonomous cycle of near-wall turbulence. *J. Fluid Mech.* **389**, 335–359.

JIMÉNEZ-GONZÁLEZ, J.I. & BRANCHER, P. 2017 Transient energy growth of optimal streaks in parallel round jets. *Phys. Fluids* **29** (11), 114101.

JOHANSSON, P.B.V. & GEORGE, W.K. 2006 The far downstream evolution of the high-Reynolds-number axisymmetric wake behind a disk. Part 2. Slice proper orthogonal decomposition. *J. Fluid Mech.* **555**, 387.

JOHANSSON, P.B.V., GEORGE, W.K. & WOODWARD, S.H. 2002 Proper orthogonal decomposition of an axisymmetric turbulent wake behind a disk. *Phys. Fluids* **14** (7), 2508.

KANG, H.S. & MENEVEAU, C. 2002 Universality of large eddy simulation model parameters across a turbulent wake behind a heated cylinder. *J. Turbul.* **3** (1), 032.

KIM, H.T., KLINE, S.J. & REYNOLDS, W.C. 1971 The production of turbulence near a smooth wall in a turbulent boundary layer. *J. Fluid Mech.* **50** (1), 133–160.

KLINE, S.J, REYNOLDS, W.C., SCHRAUB, F.A. & RUNSTADLER, P.W. 1967 The structure of turbulent boundary layers. *J. Fluid Mech.* **30** (4), 741–773.

LANDAHL, M.T. 1975 Wave breakdown and turbulence. *SIAM J. Appl. Math.* **28** (4), 735–756.

LASAGNA, D., BUXTON, O.R.H. & FISCALETTI, D. 2021 Near-field coherent structures in circular and fractal orifice jets. *Phys. Rev. Fluids* **6** (4), 044612.

LIEPMANN, D. & GHARIB, M. 1992 The role of streamwise vorticity in the near-field entrainment of round jets. *J. Fluid Mech.* **245** (-1), 643.

LU, S.S. & WILLMARTH, W.W. 1973 Measurements of the structure of the Reynolds stress in a turbulent boundary layer. *J. Fluid Mech.* **60** (3), 481–511.

LUMLEY, J.L. 1967 The structure of inhomogeneous turbulent flows. In *Atmospheric Turbulence and Radio Wave Propagation* (ed. A.M. Yaglom & V.I. Tatarski), pp. 166–178. Nauka.

LUMLEY, J.L. 1970 *Stochastic Tools in Turbulence*. Academic.

MAIA, I., JORDAN, P., HEIDT, L., COLONIUS, T., NEKKANTI, A. & SCHMIDT, O.T. 2021 Nonlinear dynamics of forced wavepackets in turbulent jets. In *AIAA Aviation 2021 Forum, AIAA paper* 2021-2277. American Institute of Aeronautics and Astronautics.

MARANT, M. & COSSU, C. 2018 Influence of optimally amplified streamwise streaks on the Kelvin–Helmholtz instability. *J. Fluid Mech.* **838**, 478–500.

MIZUNO, Y. & JIMÉNEZ, J. 2013 Wall turbulence without walls. *J. Fluid Mech.* **723**, 429–455.

MOCZARSKI, L., TRELEAVEN, N.C., OBERLEITHNER, K., SCHMIDT, S., FISCHER, A. & KAISER, T.L. 2022 Interaction of multiple linear helical modes in the turbulent flow field of an industrial fuel injection system. In *AIAA SciTech 2022 Forum, San Diego, CA, USA, AIAA paper* 2022-1061. American Institute of Aeronautics and Astronautics.

MONTY, J.P., STEWART, J.A., WILLIAMS, R.C. & CHONG, M.S. 2007 Large-scale features in turbulent pipe and channel flows. *J. Fluid Mech.* **589**, 147–156.

NEKKANTI, A., MAIA, I.A., JORDAN, P., HEIDT, L., COLONIUS, T. & SCHMIDT, O.T. 2022 Triadic nonlinear interactions and acoustics of forced versus unforced turbulent jets. In *12th International Symposium on Turbulence and Shear Flow Phenomena (TSFP12), Osaka, Japan*.

NEKKANTI, A. & SCHMIDT, O.T. 2021 Frequency–time analysis, low-rank reconstruction and denoising of turbulent flows using SPOD. *J. Fluid Mech.* **926**, A26.

NEKKANTI, A. & SCHMIDT, O.T. 2023 Gappy spectral proper orthogonal decomposition. *J. Comput. Phys.* **478**, 111950.

NEKKANTI, A., SCHMIDT, O.T., MAIA, I., JORDAN, P., HEIDT, L. & COLONIUS, T. 2023 Bispectral mode decomposition of axisymmetrically and non-axisymmetrically forced turbulent jets. In *AIAA AVIATION 2023 Forum, San Diego, CA, USA, AIAA paper* 2023-3651. American Institute of Aeronautics and Astronautics.

NIDHAN, S., CHONGSIRIPINYO, K., SCHMIDT, O.T. & SARKAR, S. 2020 Spectral proper orthogonal decomposition analysis of the turbulent wake of a disk at $Re = 50\,000$. *Phys. Rev. Fluids* **5** (12), 124606.

NIDHAN, S., SCHMIDT, O.T. & SARKAR, S. 2022 Analysis of coherence in turbulent stratified wakes using spectral proper orthogonal decomposition. *J. Fluid Mech.* **934**, A12.

NOGUEIRA, P.A.S. & CAVALIERI, A.V.G. 2021 Dynamics of shear-layer coherent structures in a forced wall-bounded flow. *J. Fluid Mech.* **907**, A32.

NOGUEIRA, P.A.S., CAVALIERI, A.V.G., JORDAN, P. & JAUNET, V. 2019 Large-scale streaky structures in turbulent jets. *J. Fluid Mech.* **873**, 211–237.

OBLIGADO, M., DAIRAY, T. & VASSILICOS, J.C. 2016 Nonequilibrium scalings of turbulent wakes. *Phys. Rev. Fluids* **1** (4), 044409.

ORTIZ-TARIN, J.L., NIDHAN, S. & SARKAR, S. 2021 High-Reynolds number wake of a slender body. *J. Fluid Mech.* **261**, 333–374.

ORTIZ-TARIN, J.L., NIDHAN, S. & SARKAR, S. 2023 The high-Reynolds-number stratified wake of a slender body and its comparison with a bluff-body wake. *J. Fluid Mech.* **957**, A7.

PATEL, H.D. & YEH, C.A. 2023 Modal analysis for three-dimensional instability coupling mechanisms in turbulent wake flows over an airfoil. In *AIAA SCITECH 2023 Forum, National Harbor, MD, USA, AIAA paper* 2023-1987. American Institute of Aeronautics and Astronautics.

PICKERING, E., RIGAS, G., NOGUEIRA, P.A.S., CAVALIERI, A.V.G., SCHMIDT, O.T. & COLONIUS, T. 2020 Lift-up, Kelvin–Helmholtz and Orr mechanisms in turbulent jets. *J. Fluid Mech.* **896**, A2.

SAMIE, M., APARECE-SCUTARIU, V., LAVOIE, P., SHIN, D. & POLLARD, A. 2022 Three-dimensional large-scale and very-large-scale coherent structures in a turbulent axisymmetric jet. *J. Fluid Mech.* **948**, A29.

SCHMIDT, O.T. 2020 Bispectral mode decomposition of nonlinear flows. *Nonlinear Dyn.* **102** (4), 2479–2501.

SCHMIDT, O.T. 2022 Spectral proper orthogonal decomposition using multitaper estimates. *Theor. Comput. Fluid Dyn.* **36** (5), 741–754.

SCHMIDT, O.T. & COLONIUS, T. 2020 Guide to spectral proper orthogonal decomposition. *AIAA J.* **58** (3), 1023–1033.

SCHMIDT, O.T., TOWNE, A., RIGAS, G., COLONIUS, T. & BRES, G.A. 2018 Spectral analysis of jet turbulence. *J. Fluid Mech.* **855**, 953–982.

SMITH, C.R. & METZLER, S.P. 1983 The characteristics of low-speed streaks in the near-wall region of a turbulent boundary layer. *J. Fluid Mech.* **129**, 27–54.

TANEDA, S. 1978 Visual observations of the flow past a sphere at Reynolds numbers between 10^4 and 10^6. *J. Fluid Mech.* **85** (1), 187–192.

THOMSON, D.J. 1982 Spectrum estimation and harmonic analysis. *Proc. IEEE* **70** (9), 1055–1096.

TOWNE, A., SCHMIDT, O.T. & COLONIUS, T. 2018 Spectral proper orthogonal decomposition and its relationship to dynamic mode decomposition and resolvent analysis. *J. Fluid Mech.* **847**, 821–867.

UBEROI, M.S. & FREYMUTH, P. 1970 Turbulent energy balance and spectra of the axisymmetric wake. *Phys. Fluids* **13** (9), 2205–2210.

WALEFFE, F. 1997 On a self-sustaining process in shear flows. *Phys. Fluids* **9** (4), 883–900.

WALLACE, J.M. 2016 Quadrant analysis in turbulence research: history and evolution. *Annu. Rev. Fluid Mech.* **48**, 131–158.

WELCH, P. 1967 The use of fast Fourier transform for the estimation of power spectra: a method based on time averaging over short, modified periodograms. *IEEE Trans. Audio and Electroacoust.* **15** (2), 70–73.

YUN, G., KIM, D. & CHOI, H. 2006 Vortical structures behind a sphere at subcritical Reynolds numbers. *Phys. Fluids* **18** (1), 015102.